PHASE IMAGING WITH COMPUTATIONAL SPECIFICTY FOR
CELL BIOLOGY APPLICATIONS

BY

YUCHEN HE

THESIS

Submitted in partial fulfillment of the requirements
for the degree of Master of Science in Electrical and Computer Engineering
in the Graduate College of the
University of Illinois Urbana-Champaign, 2021

Urbana, Illinois

Adviser:

Professor Gabriel Popescu

Abstract

Recent advancements in quantitative phase imaging (QPI) and deep learning have opened up an exciting frontier. It has been shown that deep learning methods, with their ability to extract intricate structures from massive raw datasets, can be applied to both interpreting QPI measurements of biological samples and enhancing the imaging capabilities of QPI systems. Phase imaging with computational specificity (PICS), a workflow that combines deep learning and QPI, has recently been developed to nondestructively measure biophysical parameters or markers from label-free samples directly. In this thesis, we present a new non-invasive, high-throughput method built upon the principle of PICS, to detect the cell cycle of live cell clusters. We demonstrate that the proposed method can be applied to study single-cell dynamics within the cell cycle as well as investigate cell biophysical parameter distribution across different stages of the cell cycle.

Acknowledgments

Contents

1. Introduction

1.1 Quantitative Phase Imaging

In 1665, Robert Hooke, a Fellow of the Royal Society in London, published the book

Micrographia, describing his observation of "minute bodies" using "magnifying glasses" [1]. In

this work, Hooke included an illustration of the compound lens system he used, consisting of a

light source, three optical lenses, and a moving stage. He also coined the term "cell" to describe

the porous structure he saw in plant sections [2]. It is intriguing to know what level of impact

Hooke envisioned for his book, as light microscopes remained the most commonly-used tool in

biology and medicine [2, 3] four centuries later.

Interestingly, Hooke was probably also the first scientist to report seeing stained objects

(dyed wool and hair) under a light microscope [4]. Stains and dyes are still routinely used today

to investigate specific structures within cells and tissues [5], the necessity of which came from

the fact that many biological samples (e.g. single cells and thin tissue slices) are transparent and

weakly scattering [6]. In other words, such samples do not affect the amplitude of the incident

light significantly, generating orders of magnitude weaker scattered light, hence are difficult to

see using cameras that are only sensitive to intensity.

Naturally, one direction to visualize such structures is to change their absorption

properties. In 1914, soon after the development of the first fluorescence microscope [7],

Stanislav von Provazek launched the new era of using fluorescent dyes as stains in cell biology

by reporting the study of dye binding in fixed tissues and living cells [4]. However, the

visualization capability and highly specific information of fluorescence came at expensive costs,

for example, photobleaching and phototoxicity. Photobleaching refers to all processes that cause

the fluorescent signal to decrease substantially with time and fade permanently [5, 8], yielding

low signal-to-noise ratio and limiting the applicability to experiments over a long period of time.

Lots of efforts have been invested to reduce photobleaching, including tight control over the dose

of light that reaches the sample, development of fluorophores with greater photostability, and

utilization of high-quality optical filters and cameras [8]. Unfortunately, even with all these

measures, photobleaching still cannot be fully eliminated and remains one of the most important

factors restraining future developments and application of fluorescent techniques. Besides

photobleaching, the strong light necessary to excite the fluorophore also induces phototoxicity,

which can bring morphologically imperceptible damage to cellular macromolecules [9]. Such

damage can alter the kinetics of cellular processes, leading to irreproducible and misinterpreted

experimental data.

Another direction to visualize the weekly scattering samples, minimizing the risk of light-

induced damage that is associated with any type of fluorescence microscopy [10], is to utilize

available endogenous contrast [6]. In 1873, Ernst Abbe formulated microscopic image formation

as a complicated interference phenomenon [11]. Following this idea, Frits Zernike rendered

transparent objects visible without any stain by placing a phase strip in the focal plane of a

microscope [12] in the 1930s. The advantage of this method, later known as phase contrast

microscopy [13, 14], was extended in the 1950s, when two groups of researchers independently

reported that the refractive index is linearly proportional to cell density, regardless of

composition [15, 16]. Thus, the phase contrast microscopy measurements can provide a

qualitative view of the dry-mass distribution of the sample. Phase contrast microscopes remain

broadly used in biology laboratories for quickly inspecting live samples. In 1948, Dennis Gabor

introduced the idea of formulating imaging as a form of information transmission by

demonstrating that both the amplitude and the phase information of the field at the focus plan can be recorded in one photographic recording [17], opening up an active field of research known today as *holography* [18-20].

Quantitative phase imaging (QPI) [6, 21], built upon the ideas of Abbe, Zernike, and Gabor, emerges as a family of label-free methods that can image completely transparent cells and tissues and report quantitatively the refractive index and thickness distribution associated with the specimen. In recent years, various QPI instruments have been developed and applied to both basic and clinical science [6, 22]. QPI methods have been used to reveal red blood cells morphology [23-27], monitor cell growth [28-34], measure cell membrane fluctuations [35-37] and intracellular transport [38-40], image unlabeled microtubules [41, 42], study neuronal networks [43-45], assay sperm cell motility [46-48], and extract intrinsic markers for cancer diagnosis and prognosis [49-51]. Recently QPI methods have also been extended to optically thick samples, such as embryos, brain slices, and spheroids [52, 53], as well as three-dimensional (3-D) tomography [54-58]. Although QPI methods provide sensitivity to nanoscale changes, they suffer from a lack of chemical specificity, meaning it is difficult to pinpoint various types of sub-cellular structures captured in the optical path delay maps. Such difficulty stems from the difficulty with mapping the refractive index (RI) distribution to the chemical composition of different molecular species [59].

1.2 Deep Learning

The last two decades have witnessed another dramatic revival of a classic research field: deep learning, a subfield of artificial intelligence [59]. Deep learning is a form of representation learning, where a general-purpose learning procedure is employed to automatically extract features from raw datasets [60]. The key ideas behind deep learning, i.e., feedforward neural

networks [61] and backpropagation algorithms [62, 63], have been proposed since the 1970s. However, due to the widely-held belief that prior knowledge is indispensable to learning good features, deep learning was largely deserted by the community in the 1990s. It was not until around 2006, when researchers reported that deep feedforward networks performed very well in recognizing human face, handwritten digits [64], and pedestrians [65], that the interest in neural networks was reignited. An important factor to the resurgence of neural networks was the advent of powerful programmable graphical processing units (GPUs) [66], which helped reduce the training time of neural networks from days to hours [67]. The neural network based methods were quickly transferred from computer vision to speech recognition and refreshed state-of-art performance for large-vocabulary speech recognition tasks [68] as well.

As more groups started applying deep neural networks, it was soon discovered that one type of deep network, the convolutional neural network (ConvNet) [69], was noticeably easier to train and generalize better, especially compared to networks with only fully connected layers [60]. Inspired by the biological structure of cells discovered in visual neuroscience [70, 71], ConvNets were able to take advantage of the hierarchy presented in many natural signals via sharing weights within feature maps, applying local connections to capture motifs that are formed by highly correlated adjacent group of values, and using pooling layers to capture semantically similar motifs and creating invariance to shifts and distortions [60, 72]. Since the ImageNet competition in 2012 [73], when AlexNet [74] reported ground-breaking 15.3% top-5 test error, ConvNets have become the mainstream methods for object detection, semantic segmentation, and image recognition [75-77].

With QPI's ability to generate uniform, high-quality data and deep learning's capability of discovering intricate features and structures in large datasets, it would be natural to combine

4

the best of both worlds and utilize deep learning models to interrogate QPI data for information that might not be obvious to traditional imaging processing methods. In 2017, researchers from Korea Advanced Institute of Science and Technology demonstrated one of the first applications of deep learning on QPI data, using ConvNets to classify anthrax spores in phase images [78]. Later on, researchers from the University of California, Los Angeles showed that ConvNets can transform QPI data into their histologically stained bright-field counterparts [79]. In the general light microscopy field, deep learning has also been used to computationally stain biological samples from bright-field images or traditional phase contrast images [80, 81]. Inspired by this exciting frontier, phase imaging with computationally specificity (PICS) [82], a workflow that combined deep learning models with QPI methods, was developed to extract biophysical parameters and markers from label-free samples directly [83-85].

Besides the extraordinary capability to interpret QPI data [78, 86, 87] , deep learning methods have also been proven effective for solving inverse problems [88] or enhancing the QPI imaging systems [59]. This type of applications, usually referred to as computational imaging or image transformation [89], focuses on utilizing ConvNets to extract information about the imaging physics while remaining agnostic to the samples presented. In 2017, a ConvNet based method to solve the inverse problem was presented and it was able to perform upsampling and deblurring simultaneously, generating a high-resolution image from a low-resolution image [90]. ConvNet based methods were also recently developed to achieve image reconstruction with a single-shot in-line holography over an extended depth of field [91], reconstruct three-dimensional (3-D) RI tomography [92], perform auto-focusing [93, 94], compensate for phase aberration [95], and suppress coherent or speckle noise [96, 97].

1.3 Structure of the Thesis

In this thesis, we present some of our recent works at the intersection of QPI and deep learning. First, we describe the QPI systems used for imaging experiments (Chapter 2). Then we outline the principle of PICS and present its application in cell growth study and reproductive outcome prediction (Chapter 3). We also report the capability of deep learning to enhance QPI imaging systems (Chapter 4). Finally, we present a new non-destructive, high-throughput cell cycle classification workflow (Chapter 5).

2. Quantitative Phase Imaging

As introduced in Chapter 1, quantitative phase imaging (QPI) is a family of label-free imaging methods that has gained significant interest in recent years due to its applicability to both basic and clinical science. In this chapter, we first discussed the figures of merit of QPI systems and then outlined the principles of three different QPI methods that were used for the imaging experiments presented in this thesis.

2.1 Full-field QPI and Figures of Merit

The full-field QPI methods [6, 21, 98] can be categorized into two classes: off-axis [99-106] and phase shifting [52, 53, 107-112]. Off-axis interferometry exploits spatial phase modulation and can produce a phase map from a single intensity recording, whereas phase-shifting interferometry controls the time delay of the reference field to record multiple (at least three) intensity images to extract the phase map associated with the object [6].

The main figures of merit to quantify the performance of QPI methods are: acquisition rate, transverse resolution, temporal phase sensitivity, and spatial phase sensitivity [21]. In general, off-axis QPI methods provide faster acquisition rate, while phase-shifting interferometry are more likely to preserve the diffraction-limited transverse resolution. Phase sensitivity defines the smallest phase shift a QPI method can detect. This figure of merit can be quantified by measuring a stable sample and then calculating the standard deviation of the phase measurements (see Section 8.5 of Ref [21]). Temporal phase sensitivity is governed by the phase stability of the QPI method and the spatial phase sensitivity is limited by the amount of background noise present. Common-path QPI methods, where the reference field and the scattered field travel along physically close paths, usually provide better phase stability and temporal phase

sensitivity. White-light QPI methods, where a broad optical spectrum illumination is used, yield images with lower spatial intensity fluctuations, thus better spatial phase sensitivity.

2.2 Diffraction Phase Microscopy

Diffraction phase microscopy (DPM) is an off-axis, common-path and single-shot QPI method that utilize a compact Mach-Zehnder interferometer system to alleviate common phase noise problems due to mechanical vibration and air fluctuation [99-101, 113-118]. Figure 1 presents the system schematic of DPM, where a phase grating and a $4f$ lens system is appended to the output port of a conventional microscope.
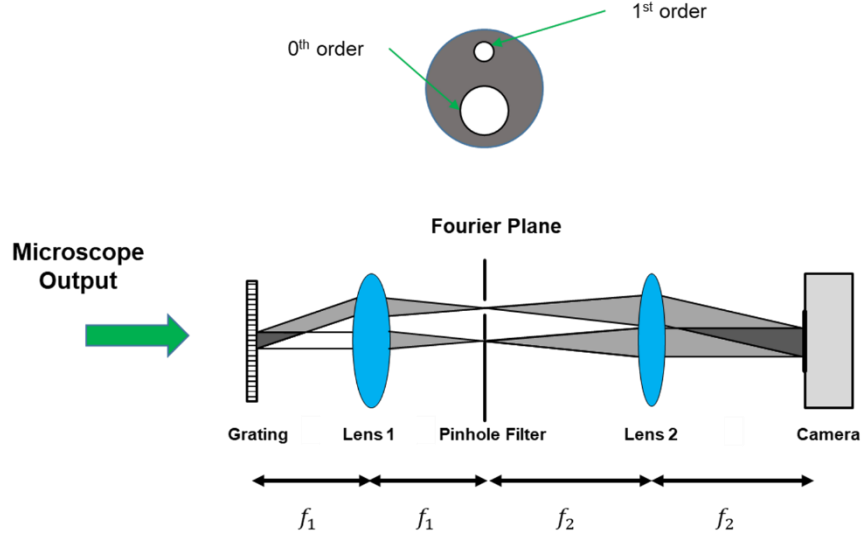
Figure 1. DPM Schematic. The DPM system consists of a phase grating and a $4f$ lens system with a pinhole filter.

Let U_0 denote the 0th order field and U_1 denote the 1st order field. Notice we are only concerned with these two fields as the other orders from the grating either do not pass Lens L1 or get filtered out in the Fourier plane. The optical field at the grating plane can be expressed as

$$U_{GP}(x, y) = U_0(x, y) + U_1(x, y)e^{i\beta x} \tag{2.1}$$

where $\beta = \frac{2\pi}{\Lambda}$ and Λ is the grating period.

Lens L1 performs a Fourier transform of the field and thus the field at the Fourier plane, before the pinhole filter can be expressed as Equation (2.2). The shifting theorem of Fourier transform is applied to simplify the term involving $\widetilde{U_1}$.

$$\widetilde{U}_{FP-}(k_x, k_y) = \widetilde{U_0}(k_x, k_y) + \widetilde{U_1}(k_x - \beta, k_y) \tag{2.2}$$

$k_x = \alpha x_1$ where x_1 denotes the coordinate at the Fourier plane and $\alpha = \frac{2\pi}{\lambda f_1}$. k_y is defined similarly. At the Fourier plane, the pinhole filter allows the full 0th order to pass and filters down the 1st order such that the field becomes a uniform plane wave after lens L2. Thus, the field after the filter can be expressed as

$$\widetilde{U}_{FP+}(k_x, k_y) = \widetilde{U_0}(k_x, k_y) + \widetilde{U_1}(0,0)\delta(k_x - \beta, k_y) \tag{2.3}$$

Notice the property of delta function $f(x)\delta(x - x_0) = f(x_0)\delta(x - x_0)$ is used to simplify the product of $\widetilde{U_1}$ and the transfer function of the filter.

Lens L2 performs a second Fourier transform and we have the filed at the camera plane as

$$U_{CP}(x, y) = \frac{1}{|\alpha|}[U_0\left(-\frac{x}{M}, -\frac{y}{M}\right) + U_1(0,0)e^{i\frac{\beta x}{M}}] \tag{2.4}$$

Here $M = -\frac{f_2}{f_1}$ denotes the magnification introduced by the $4f$ lens system.

Let $A_{0,1}$ and $\phi_{0,1}$ denote the amplitude and phase of the 0th and 1st order field, respectively. We can rewrite Equation (2.4) as

$$U_{CP}(x, y) = \frac{1}{|\alpha|}\left\{A_0\left(-\frac{x}{M}, -\frac{y}{M}\right)e^{i\phi_0\left(-\frac{x}{M}, -\frac{y}{M}\right)} + A_1(0,0)e^{i\left[\phi_1(0,0)+\frac{\beta x}{M}\right]}\right\} \tag{2.5}$$

The field at the camera is essentially an interferogram between two magnified copies of the image, where one contains all the information (0th order) and the other is filtered down to DC as

a reference field (1st order). To simplify the notation, we define $x' = -\frac{x}{M}$ and $\Delta\phi = \phi_0(x', y') - \phi_1$. And the irradiance detected by the camera can thus be expressed as

$$I_{CP}(x', y') = I_0(x', y') + I_1 + 2\sqrt{I_0(x', y')I_1}\cos(\beta x' + \Delta\phi) \tag{2.6}$$

To reconstruct the phase information, we can first isolate the cosine term in Equation (2.6) and then formulate it as the real part of a complex analytical signal and retrieve the imaginary prat of that signal via a Hilbert transform, as denoted in Ref [102]

$$\sin(\beta x' + \Delta\phi) = P\int \frac{\cos(\beta x'' + \Delta\phi)}{x' - x''} dx'' \tag{2.7}$$

Then the phase information associated with the object is extracted as

$$\Delta\phi = \tan^{-1}\left[\frac{\sin(\beta x' + \Delta\phi)}{\cos(\beta x' + \Delta\phi)}\right] - \beta x' \tag{2.8}$$

Practically, this operation can be implemented by taking the Fourier transform of the interferogram, selecting only one side of the Fourier spectrum, moving it to the baseband, and taking the inverse Fourier transform back to the spatial domain [101, 113].

Since these integral operators are computationally demanding, researchers have parallelized these operations using compute unified device architecture (CUDA) [66, 119] and GPUs and successfully achieved video rate performance for mega-pixel images [120]. Besides utilizing hardware acceleration, a derivative method for phase reconstruction has also been proposed in [121]. This method retrieves the phase information by numerically calculating the transverse 1st and 2nd order derivatives of the interferogram, thus providing a four-time speed up compared to traditional Hilbert transform based approach [121].

Recently, white-light DPM (wDPM) [100] has also been developed, where a spatially coherent white-light halogen lamp replaces the laser. The reference beam is created by closing down the condenser numerical aperture (NA) and filtering the 0th order beam with a pinhole

mask that matches the condenser NA. Thus, the reference beam is now a low-pass-filtered version of the sample beam.

DPM has been widely applied to both materials [115-117] and life sciences [100, 113, 114]. Its common-path architecture ensures phase stability against noise, thus providing high temporal phase sensitivity, while its off-axis geometry allows single-shot measurement as fast as the camera detector permits. With wDPM, the system can be easily attached to existing conventional microscopy without changing illumination. With recent advancements in CUDA and GPU computing, DPM measurements can be performed to extract quantitative information in real time [101].

2.3 Spatial Light Interference Microscopy

Spatial light interference microscopy (SLIM) [42, 45, 108, 109, 122-127] is a phase-shifting common-path QPI method that can be implemented as an add-on module to a commercial phase contrast microscope. The SLIM schematic is illustrated in Fig. 2. The phase ring, which provides $\pi/2$ attenuation in traditional phase contrast microscopy [13], is imaged via Lens L1 onto the spatial light modulator (SLM) plane. By controlling the voltage applied to the SLM via a software package developed in house, we recorded four intensity images corresponding to phase shifts of $0, \pi/2, \pi$, and $3\pi/2$ between the scattered field and the incident field. We denote the incident field as U_0 and the scattered field as U_1. The field at the camera plane can be expressed as

$$U(x, y, k) = |U_0|e^{i\phi_0} + |U_1(x,y)|e^{i(\phi_0 + \Delta\phi(x,y) + \frac{k\pi}{2})} \tag{2.9}$$

where ϕ_0 denotes the phase of the incident field; $k = 0,1,2,3$; and $\Delta\phi(x,y)$ denotes the phase difference between the incident field U_0 and the scattered field U_1. The intensity detected by the camera can thus be written as

$$I(x, y, k) = |U_0|^2 + |U_1|^2 + 2|U_0||U_1(x,y)|\cos[\Delta\phi(x,y) + \frac{k\pi}{2}] \qquad (2.10)$$

The phase difference can be retrieved following reported procedures [107-109] as

$$\Delta\phi(x,y) = \tan^{-1}\left[\frac{I(x,y,3) - I(x,y,1)}{I(x,y,0) - I(x,y,2)}\right] \qquad (2.11)$$

Now the phase distribution associated with the image (difference between the total field and the incident field) can be extracted following Equation (2.12 – 2.14). Assuming no additional phase shift is introduced ($k = 0$), we can write the interferogram as Equation (2.12).

$$U(x,y) = |U_0|e^{i\phi_0} + |U_1(x,y)|e^{i(\phi_0+\Delta\phi(x,y))} \qquad (2.12)$$

If we denote $\beta(x,y) = |E_1(x,y)|/|E_0|$, we can rewrite Equation (2.12) into Equation (2.13).

$$U(x,y) = |U_0|e^{i\phi_0}\left[1 + \beta(x,y)e^{i\Delta\phi(x,y)}\right] \qquad (2.13)$$

Namely,

$$U(x,y) = |U_0|e^{i\phi_0}\left[1 + \beta(x,y)e^{i\Delta\phi(x,y)}\right] \qquad (2.14)$$

$$= |U_0|\{[\cos\phi_0 + \beta\cos(\phi_0 + \Delta\phi(x,y))] + i[\sin\phi_0 + \beta\sin(\phi_0 + \Delta\phi(x,y))]\}$$

Now we can retrieve the total phase as in Equation (2.15). Notice since the incident field U_0 is used as reference, ϕ_0 essentially becomes 0. The amplitude ratio $\beta(x,y)$ can be obtained from the four intensity recordings directly without additional measurements (see Ref [107]).

$$\phi(x,y) = \tan^{-1}\left[\frac{\beta(x,y)\sin\Delta\phi(x,y)}{1 + \beta(x,y)\cos\Delta\phi(x,y)}\right] \qquad (2.15)$$

Due to the white light illumination used and thus the lack of speckle noise, SLIM measurements have better spatial uniformity and accuracy compared to those of DPM [108, 109]. However, since such illumination is not perfectly spatially coherent, SLIM images are affected by the "halo" artifact, which refers to the phenomenon of missing low frequencies in the measured phase map [128]. Numerical processing approaches have been proposed to correct

halos in real time [129, 130]. Figure 2b presents an example of the scattered phase map

(Equation (2.11)), total phase map (Equation (2.15)), as well as the halo-free phase map.
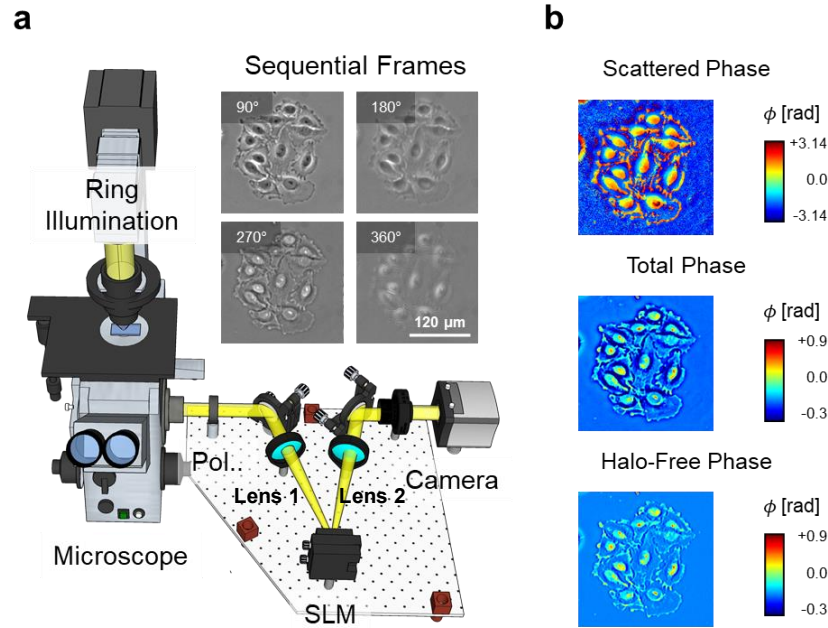
Figure 2. SLIM Principle. (a) The ring illumination is matched to the objective's back focal plane and the mask on the spatial light modulator (SLM), effectively resulting in a phase-contrast microscope with a variable retardance ring. Four frames are recorded, corresponding to increments of 90 degrees introduced by the SLM. (b) SLIM image reconstruction and the halo-removed SLIM image. Adapted from Ref [82] with permission.

SLIM has been successfully applied to study cell dynamics [131], cell growth [30, 33],

cell migration [132], and dry mass transport [38]. Besides basic science applications, SLIM has

also been used to perform cancer screening [133, 134], cancer diagnosis and prognosis [135,

136], blood testing [137] , as well as to assist reproductive studies [138]. SLIM measurements

have been used to solve for the scattering potential under the first-order Born approximation

[56], extending the QPI measurements to three-dimensional (3-D). Recently, Wolf phase

tomography (WPT) [139], a fast 3-D RI construction method based on the Wolf equations for

propagation correlations of partially coherent light [140] is developed. This method can decouple

the RI information from the sample thickness directly in the space-time domain from three

independent SLIM measurements corresponding to each phase shift, which can be employed to develop RI-based cell classification methods or fiber tracking methods.

2.4 Gradient Light Interference Microscopy

Gradient light interference microscopy (GLIM) [52, 53] is a common-path, phase-shifting and white-light QPI methods that generate phase maps with nanometer pathlength stability, speck-free quality, and diffraction-limited resolution. Just as SLIM upgrades a conventional phase contrast microscope, GLIM upgrades a conventional differential interference contrast (DIC) [141] microscope via phase-shifting interferometry. The system schematic of a GLIM module is illustrated in Fig. 3.
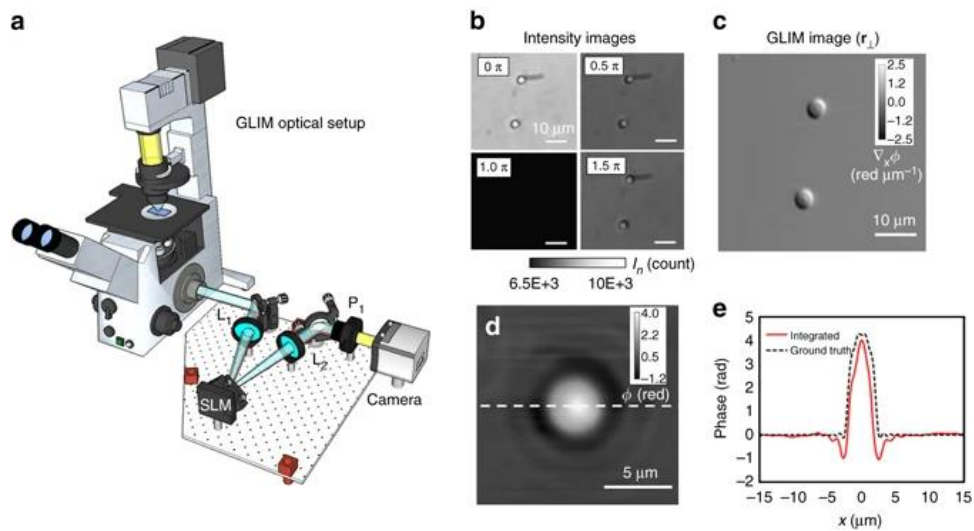
Figure 3. GLIM Principle. (a) GLIM optical setup. (b) Four frames are acquired by the GLIM module, one for each phase shift applied by the SLM. (c) Extracted quantitative-gradient map of two 3 µm polystyrene beads immersed in oil. (d) Integrated phase map of a 4.5 µm polystyrene microbeads at $NA_{con} = 0.09$. (e) Cross-sections of the reconstructed phase and the computed ground truth (*black dashed curve*). Reprinted from Ref [52] with permission.

As in typical DIC microscope, a Wollaston prism is used to generate two replicas of the image field, transversely shifted by a distance δr smaller than the diffraction spot. Both fields are Fourier transformed by lens L1 to its back focal plane. The SLM, with its active axis aligned to the polarization of one field, introduces an extra phase shift of $\frac{k\pi}{2}$ for $k = 0,1,2$, and 3. Both

fields are then Fourier transformed by lens L2 to the camera plane, where a linear polarizer is aligned at 45° with respect to both fields. The interferogram at the camera plane can thus be expressed as in Equation (2.16). The irradiance detected by the cameras is expressed as in Equation (2.17) where $\gamma(r, \delta r) = \langle U^*(r)U(r + \delta r) \rangle_t$ is the mutual intensity of the temporal cross-correlation function between the two fields.

$$U(r, k) = U(r) + U(r + \delta r)e^{\frac{ik\pi}{2}} \tag{2.16}$$

$$I(r, k) = I(r) + I(r + \delta r) + 2|\gamma(r, \delta r)| \cos[\Delta\phi(r) + \frac{k\pi}{2}] \tag{2.17}$$

Using the same method described in Equation (2.11), we can solve for the phase difference between the two fields as $\Delta\phi(r) = \tan^{-1}\left[\frac{I(r,3)-I(r,1)}{I(r,0)-I(r,2)}\right]$, which renders the phase gradient along the direction of the transverse shift $\nabla_x\phi(r) \approx \Delta\phi(r)/\delta x$. To retrieve the actual phase map, we perform integration along the gradient direction, as shown in Equation (2.18).

$$\phi(x, y) = \int_0^x [\nabla_x\phi(x', y)]dx' + \phi(0, y) \tag{2.18}$$

The transverse offset δr is usually not publicly listed by the microscope manufacturer and thus needs to be estimated using a known calibration sample (e.g., beads) [52, 142]. Notice that an inaccurate δr might introduce a uniform shift of the measured phase values. Figures 5b-c shows an example of the four intensity images acquired and the quantitative phase gradient map. The integrated phase map is presented in Fig. 3d with the comparison of phase values presented in Fig. 3e.

As a QPI method, GLIM is suitable for quantifying the growth and proliferation of adherent cell cultures over a large temporal scale. Dispersion phase spectroscopy (DPS) method

15

can also be used to analyze GLIM measurements for cellular mass transport investigation [40, 52]. Unlike previously mentioned QPI methods, GLIM has strong sectioning capabilities due to the high numerical aperture illumination, thus able to perform tomographic imaging of thin and thick samples. Since the two interfering fields in GLIM are only shifted by a small distance laterally, they suffer equally from multiple scattering of thick samples. As a result, by taking multiple intensity images with the same incoherent background, GLIM is able to reject much of the multiple scattering contribution and produces high contrast measurements on thick samples (e.g., embryos, brain slices, spheroids, and organoids). GLIM has been applied to image bovine embryos over several days [52], to study the development of 3-D cellular architectures [40], and to monitor reactivation of latent human immunodeficiency virus (HIV) [143] . Recently, GLIM was also extended to an epi-illumination set up to facilitate imaging of biological structures that would be difficult in transmission [53].

3. Phase Imaging with Computational Specificity

In recent years, in part due to the continuous decline of computing power cost, development of frameworks for dataflow representation as well as a steep increase in data generation, deep learning techniques have been translating from consumer to scientific applications (see Chapter 1 and Ref [59, 60]). For example, it has been shown that AI can map one form of contrast into another, a concept coined as image-to-image translation [79-81, 144], which provides a data driven approach to estimate the fluorescence stain from unlabeled specimen. One of the first applications of this strategy was to estimate histological staining from QPI [79] or autofluorescence [145] signals of tissues. In those works, a separate microscope was employed to collect the stained brightfield images followed by a semi-automatic image registration step. A similar methodology was used to convert holographic microscopy images of isolated sperm cells to their virtually stained counterparts [146]. As in previous work, the stain was estimated on dead cells as a purely computational post-processing step.

3.1 Motivation

Inspired by this exciting frontier, we present phase imaging with computational specificity (PICS) [82], a combination of quantitative phase imaging and deep learning, which provides information about unlabeled live cells with high specificity. We believe PICS has several advantages compared to the previously reported methods. First, instead of focusing on fixed cells or tissue, our method (PICS) can be applied to live mammalian cell cultures, which are only possible through label-free imaging. Second, PICS performs automatic annotation by recording both QPI and fluorescence microscopy of the same field of view, on the same camera. The two imaging channels are integrated seamlessly by our software that controls both the QPI modules, fluorescence light path, and scanning stage. As a result, the colocalization of phase and

fluorescence channels came with little to none cost, meaning all the phase images were already annotated with fluorescence ground truth during acquisition, ready for deep learning training. Also, since this multimodal investigation can be extended to multiple fluorescence channels simultaneously, PICS can also be developed for multiple fluorophores at little extra cost. Third, PICS can perform real-time inference. Once the deep learning model is optimized, we incorporated it into the acquisition software, allowing users to see computational specificity during new experiments. The inference turns out to be faster than the image acquisition rate in SLIM and GLIM (limited by the four-frame modulation of SLM). Fourth, using the specificity maps obtained by computation, we can exploit the QPI channel to compute the dry mass associated with particular subcellular structures. For example, using this procedure, we demonstrated the measurement of growth curves of cell nuclei vs. cytoplasm over several days, nondestructively (see Section 3.3). PICS has also been successfully applied to predict reproductive outcomes [83], investigate neuronal growth [85], assay cell viability [84], and detect cell cycle progression (see Chapter 5).

3.2 PICS Principle

A complete PICS workflow encompasses three major steps: acquiring development and application dataset, optimizing the deep learning algorithm, and deploying the trained model for applications. The principle of each step is explained below.

3.2.1 Data Acquisition

The PICS methodology is outlined in Fig. 4. We use an inverted microscope (Axio Observer Z1, Zeiss) equipped with a QPI module (CellVista SLIM Pro and CellVista GLIM Pro, Phi Optics, Inc.) to acquire both QPI and fluorescence images simultaneously (Fig. 4a). There are multiple possible patterns to design the training data acquisition experiments. Figure 4b illustrates one

18

such pattern following a last in, first out (LIFO) order. We first imaged one time-lapse dataset D_1 containing unstained cells on QPI channel only for over five days. Then we applied staining and fixation on these cells and imaged the second dataset D_2 with both QPI and fluorescence channels. During data analysis, we used the later imaged dataset D_2 first to train a deep neural network from the colocalized QPI and fluorescence image pairs. Then we applied the trained network back on the first imaged dataset D_1 to perform digital staining (Fig. 4c) and extract biophysical parameters (e.g., dry mass and area) directly from label-free data. Finally, we deployed the trained neural network into the acquisition software (Fig. 4d), such that the computational specificity can be exploited during future experiments.
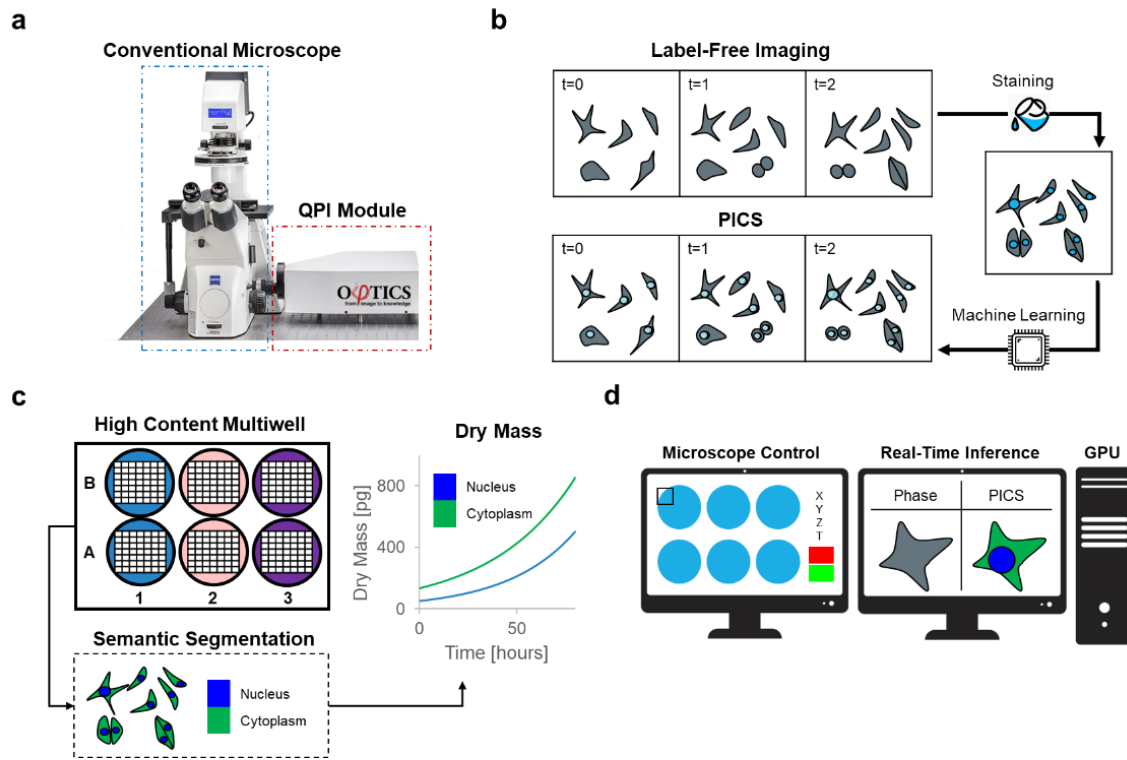
Figure 4. PICS Workflow. (a) We upgrade a conventional transmitted light microscope with a quantitative phase imaging add-on module. (b) To avoid the intrinsic toxicity of fluorescent stains, we develop a two-step protocol imaging protocol where label-free images are recorded followed by fixation and staining. From the toxic stain recorded at the end of the experiment, we train a neural network capable of digitally staining the time-lapse sequence, thus enabling time-lapse imaging of otherwise toxic stains. (c) The digital stain is used to introduce specificity to label-free imaging. (d) The PICS method is integrated into a fully automated plate reading instrument capable of displaying the machine learning results in real-time. Reprinted with permission from Ref [82].

19

We note that this LIFO pattern of image acquisition might not be suitable for some applications, e.g., cell viability [84] or cell cycle progression (see Chapter 5). For cell viability problems, if we image the training dataset only on the fixed cells toward the end of the experiments, the training dataset will suffer from severe class imbalance since all the cells become dead. For cell cycle progression, a similar problem will occur since fixed cells will not provide information about dynamic biological processes. Thus, a first in, first out (FIFO) pattern is more suitable for such applications. To be more specific, we first image a dataset D_1 with labelled cells under QPI and fluorescence channels. The imaging period will inevitably be shorter due to phototoxicity [9]. Based on the image pairs in D_1, we develop a deep neural network. Then we image a second dataset D_2 with unlabeled cells under QPI channel and applied the trained network on it for specificity.

Depending on the application and interpretation of fluorescence images, a post-processing step may also be appended to the image acquisition procedure. For instance, if the intensity level of the fluorescence signal provides additional information [82, 85], it makes sense to feed in raw fluorescence images as the ground truth to train the neural network. However, if the fluorescence signal is only used to pinpointing structures or indicating states and the intensity can vary across time or is sample-dependent [84, 147, 148], it is better to perform thresholding on the raw fluorescence images and feed in resulting segmentation masks as the ground truth. In the cases when the samples are extremely sensitive to phototoxicity or when it is difficult to find a dye that is specific enough, we inevitably need to perform manual annotation. We note that by an incremental annotation approach, we were able to get accurate ground truth data more efficiently (see Section 3.4). Figure. 5a presents the GLIM optical setup (see Section 2.4 for

details). Figure. 5b gives an example of the acquired images consisting of two fluorescence channels (cell nuclei marked by DAPI and membrane marked by DiI in this case) and GLIM.

3.2.2 Deep Learning Development

For deep learning, we developed models based on the classic U-Net architecture [149], which has been proven quite successful in many biomedical applications [150]. Fig. 5c gives an example of a modified U-Net architecture with three major changes, utilized to infer DAPI and DiI stains from GLIM images [82]. First, following the work by Google [151], we added batch normalization layers before all the activation layers, which helped accelerate the training. Second, we greatly reduced the number of parameters in our network by changing the number of feature maps in each layer of the network to a quarter of what was proposed in the original paper [149]. This change greatly reduced GPU memory usage and improved inference time, without loss of performance. Our modified U-Net model used approximately 1.9 million parameters, while the original architecture had over 30 million parameters. Third, we utilized the advantage of residual learning [152] with the hypothesis that it is easier for the models to approximate the mapping from phase images to the difference between phase images and fluorescence images than directly to fluorescence images. Thus, we implemented an addition operation between the input and the output of the last convolutional block to generate the final prediction. We noticed that this change enabled us to have much better performance under the same training conditions. Fig. 5d shows the result of the inference. Besides tuning the network architecture hyperparameter, other training strategies to enhance network performance include incorporating a pre-trained classification network with the U-Net (explored in Chapter 5), engineering better loss functions (explored in Chapter 5), and utilizing general adversarial networks (GANs) [79, 85, 91, 144, 145].

Inspired by previous works on bright-field images [80], we generate training dataset consisting of three images of each unique field of view (one in-focus, two slightly out of focus spaced 2-3 depths of field apart). We believe this approach serves as a natural form of data augmentation. We also noticed that it helps to train the network on a randomly sample sub-region from the input images during each epoch (see Chapter 4).

Despite the superior performance, the interpretability of deep learning approaches remains a big concern [153, 154], especially when applied to biomedical tasks. Many methods have been proposed recently to visualize what happens during the decision-making process inside a trained neural network black box [155]. Figure 6 presents, as an example, the intermediate representations within our network trained to infer DAPI stain from GLIM images. It can be seen that the U-Net architecture makes use of both textures inside the cell (leftmost, first layers) and spatial information such as the edges around the cellular nucleolus (bottom layers). For semantic segmentation tasks, it is also possible to visualize what regions of the images contributes to the classification of each class [156]. It has also been advocated recently to incorporate interpretability as one figure of merit to any deep learning models [157] such that we train models with interpretable design in the first place.
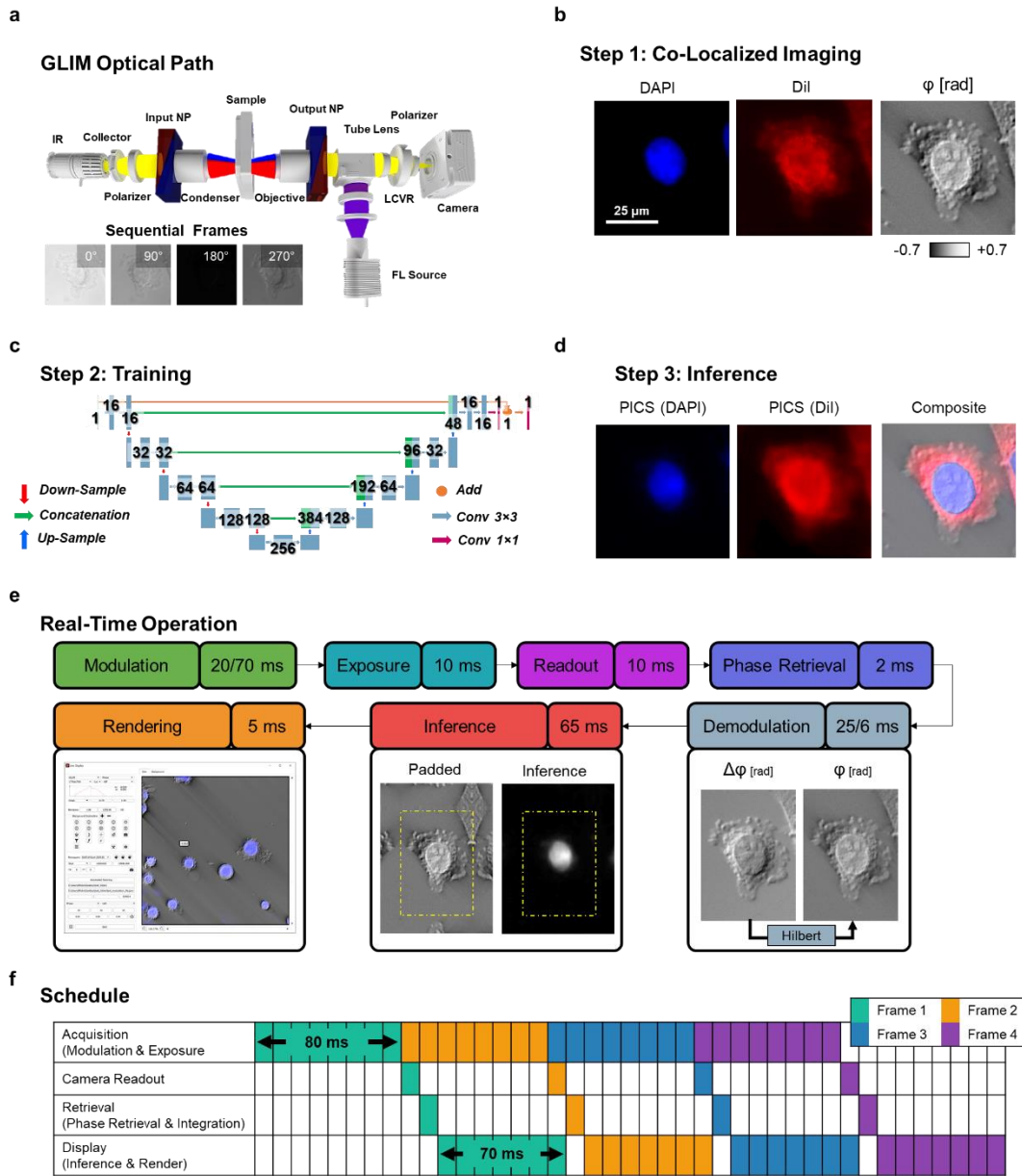
Figure 5. PICS Components. (a) GLIM module (b) Zoomed portion of a field of view showing a typical SW620 cell (20x/0.8) under DAPI, DiI, and GLIM. (c) U-Net architecture. (d) Real-time inference using optimized deep neural networks. (e) Real-time workflow with acquisition and inference. (f) Optimally overlapping computation with acquisition. Reprinted with permission from Ref [82].

Convolution
Addition
Up-Sampling + Convolution
Max Pooling
Concatenation
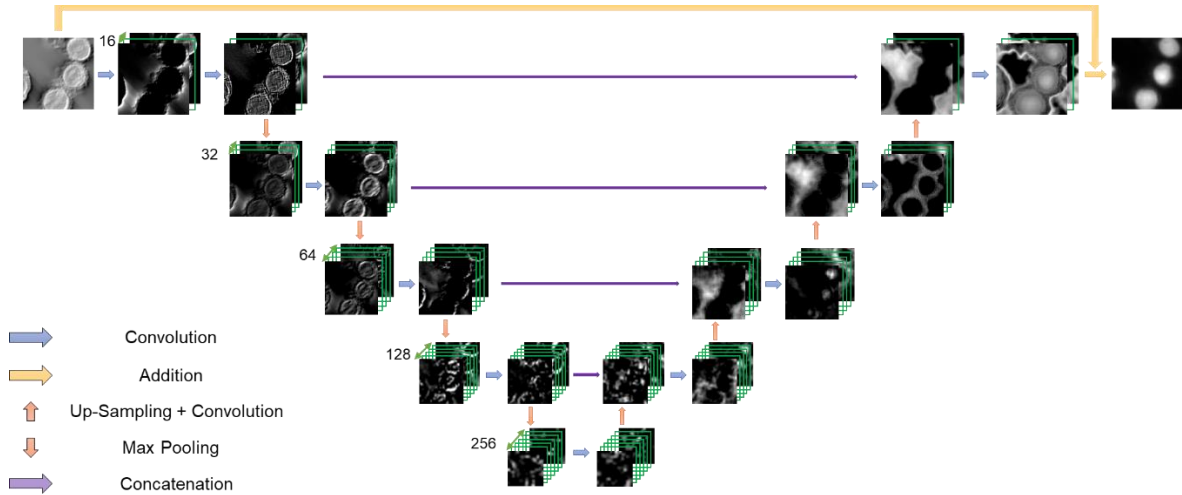
Figure 6. Interpretability of PICS-DAPI model. Reprinted with permission from Ref [82].

3.2.3 Deep Learning Deployment

To deploy our trained neural networks into acquisition and achieve real-time inference, we use

TensorRT (NVIDIA) [158, 159] which automatically tunes the inference pipeline for the specific

network architecture and GPU pairings [158]. It avoids kernel launch overhead by merging them

when possible and achieves optimal memory bandwidth by tuning the work per element in the

kernels. In addition to performance gains, TensorRT can operate directly on GPU memory,

avoiding redundant data copies and simplifying integration with existing codes.

There are three ways to load a trained model into TensorRT: via an ONNX file [160], via

a UFF file [158], or via an HDF5 file [161]. At the time of [82], TensorRT libraries lack support

for the upsampling operation used extensively in the U-Net architecture. As a result, we had to

implement a custom layer for the upsampling operation and then instrument the entire network

architecture, layer by layer, using the TensorRT C++ API. While this process was tedious, the

same network without modifications runs approximately 50% faster compared to TensorFlow

[162] (conventional approach). We also found that TensorRT stores weights in a different format

than TensorFlow. Thus, we developed a script to convert the model from TensorFlow (Google)

24

to the optimized TensorRT inference engine (NVIDIA). In short, this script transposes the weights learned by TensorFlow to match the format supported by TensorRT. Newer versions of TensorRT and ONNX have added in support for upsampling. For new projects [84], we only needed to convert a trained TensorFlow model into ONNX format and the TensorRT parser could construct the entire inference pipeline form there.

The PICS inference framework is designed to account for differences between magnification and camera frame size. Differences in magnification are accounted for by scaling the input image to the networks' required pixel size using NVIDIA's Performance Primitives (NPP) library. While TensorRT is fast, the network-tuning is performed online and can take a non-negligible time to initialize (30 seconds). To avoid tuning the network for each camera sensor size, we construct an optimized network for the largest image size and extend smaller images by mirror padding. Further, to avoid the edge artifacts typical of deep convolutional neural networks, a 32-pixel mirror pad is performed for all inference using NPP (NVIDIA, Fig. 5e).

The principal modification to the acquisition procedure was to overlap computation with hardware operation (Fig. 5e). Using the threading capabilities of C++, we divide the acquisition into four steps that are performed in parallel (Fig. 5f). One thread is assigned to coordinate the acquisition which is responsible for controlling the phase modulation hardware and initiation camera exposure. A second thread waits for the image to arrive from the camera and uploads the data to the GPU. A third thread coordinates phase-retrieval and integration. Finally, a fourth thread is responsible for running inference and rendering the image into an OpenGL buffer that can be displayed by the widget kit (Qt). Importantly this procedure prevents the graphic interface

25

from stalling between computation events. Remarkably, we find that this with robust implementation PICS can often run faster than the underlying fluorescent signal.

3.3 Cell Dynamics Study via PICS

Because of the non-destructive nature of PICS, we can apply it to monitor cells over extended periods, of many days, without a noticeable loss in cell viability. This important aspect is emphasized in Fig. 7. To perform a high-content cell growth screening assay, unlabeled SW480 and SW620 cells were imaged over seven days and PICS predicted both DAPI (nucleus) and DiI (cell membrane) fluorophores. The density of the cell culture increased significantly over the seven days, a sign that cells continued their multiplication throughout the imaging. Note that, in principle, PICS can multiplex numerous stain predictions simultaneously, as training can be performed on an arbitrary number of fluorophores for the same cell type. The only price paid is computational time, as each inference channel adds, ~65 ms to the real-time inference. The computation time for one stain is completely masked by the acquisition process and multiple networks can be evaluated in parallel on separate GPUs. We also note that fluorescence tags generally require an order of magnitude more exposure time than the QPI frames, implying that our plate reader achieves higher throughput while maintaining specificity. This effect is amplified when separate exposures are used for individual fluorophores.
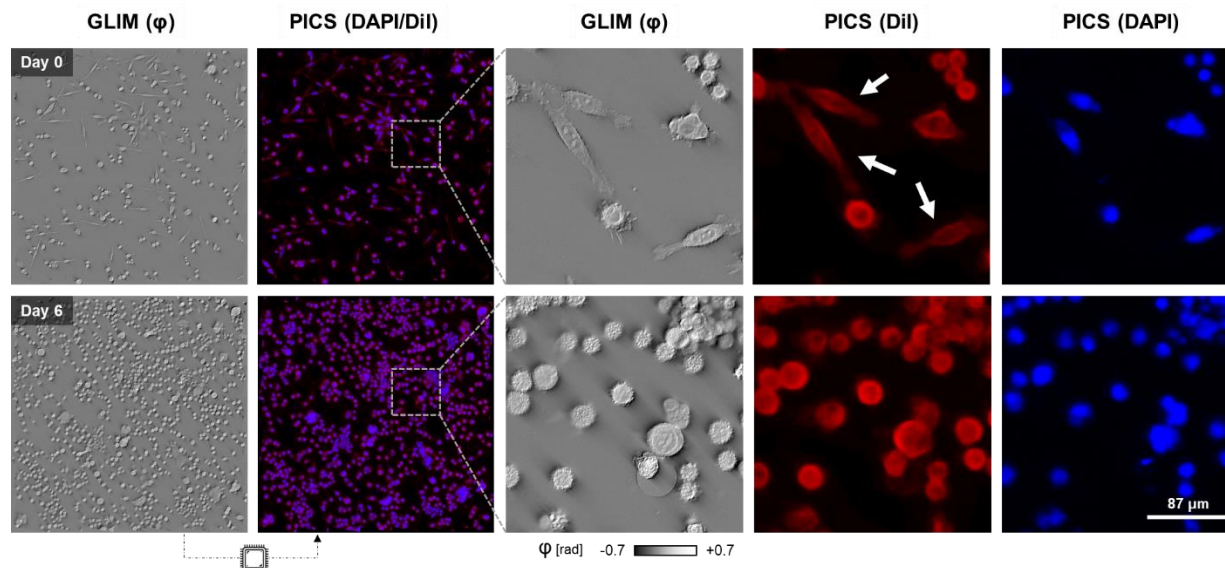
Figure 7. Time-lapse PICS of Unstained Cells. To demonstrate time-lapse imaging and high content screening capabilities, we seeded a multiwell with three distinct concentrations of SW cells (20x/0.8). These conditions were imaged over the course of a week by acquiring mosaic tiles consisting of a 2.5 mm² square area in each well using a 20x/0.8 objective. The machine learning classifier, trained at the final time point after paraformaldehyde fixation, is applied to the previously unseen sequence to yield a DiI and DAPI equivalent image. Interestingly, the neural network was able to correctly reproduce the DiI stain on more elongated fibroblast-like cells, even though few such cells are present when the training data was acquired (white arrows). Reprinted with permission from Ref [82].

We used PICS-DiI to generate a binary mask (Fig. 8), which, when applied to the QPI images, yields the dry mass of the entire cell. Similarly, PICS-DAPI allows us to obtain the nuclear dry mass. Thus, we can independently and dynamically monitor the dry mass content of the cytoplasm and nucleus. This capability is illustrated in Figs. 8b and c, where an individual cell is followed through mitosis. It is known that the nuclear-cytoplasmic ratio (NCR) is a controlling factor in embryogenesis [163] and a prognosis marker in various types of cancer [164, 165]. Figures 8d-f show the specific growth curves for a large cell field of view, consisting of a mosaic of covering a 2.5 mm² portion of a multiwell. Figure 8g illustrates the behavior of the confluence factor (defined as a fraction of the total area occupied by the cells) in time. Not surprisingly, as the confluence increases, the growth saturates due to contact inhibition[166].
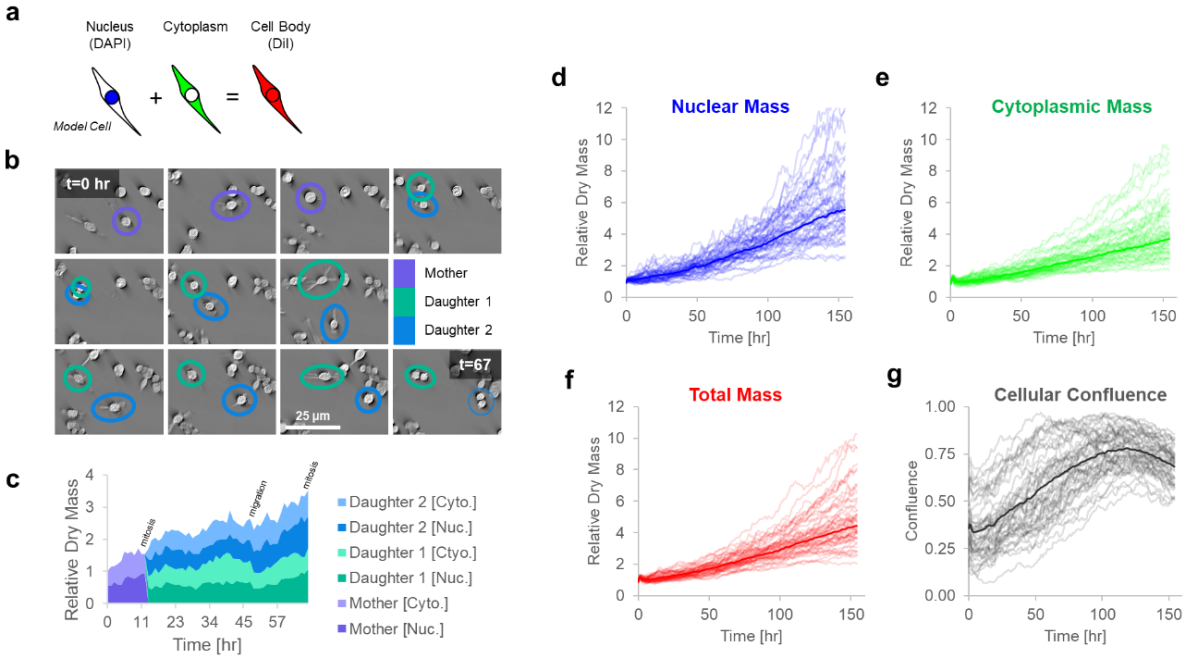
Figure 8. Tracking Dry Mass Changes in Cellular Compartments Using PICS. (a) The DiI and DAPI stains are specific to the cell body and nucleus, respectively. The difference between the two areas produces a semantic segmentation map that distinguishes between the nuclear and non-nuclear content of the cell (cytoplasm). (b) Throughout the experiment, we observe cellular growth and proliferation with cells often traveling a substantial distance between division events. (c) Using the semantic segmentation map we can track the nuclear and cytoplasmic dry mass. We find that nuclear and cytoplasmic dry mass steadily increases until mitosis, with some loss of dry mass due to cellular migration. (d-g) Semantic segmentation maps enable us to track the nuclear and cytoplasmic dry mass and area over 155 hours. The dark curve represents the median of the growth rate across forty-nine fields of view (lighter curves). The dry mass and area are normalized by the average measured value from the first six hours. In this experiment we observe that total nuclear dry mass grows faster than total cytoplasmic mass, providing further evidence that cells can divide without growing. As the cells reach optimal confluence ($t \approx 114$ hours), we observe a decrease in the growth rate of nuclear mass, although less difference in cytoplasmic dry mass growth. Reprinted with permission from Ref [82].

3.4 Reproductive Outcome Prediction via PICS

The male infertility accounts for more than 40 percent of the infertile couples [167]. The ability to evaluate sperm at the microscopic level would be useful for assisted reproductive technologies (ART), as it can allow specific selection of sperm cells for *in vitro* fertilization (IVF). For example, it has been shown that intracytoplasmic morphologically selected sperm injection (IMSI) improves the outcome of *in vitro* fertilization, as compared to the conventional intracytoplasmic sperm injection (ICSI) [168, 169]. Previous studies suggested that the anomalies unselected by IMSI are

due to abnormalities in chromatin packaging [170]. It is also important to note that the chemical reaction of the stain or label and the required fixative change the shape and size of spermatozoa [171-173]. Due to the potential toxic effects of fluorophores, morphology of sperm cells is observed using intrinsic contrast microscopy, such as differential interference contrast (DIC) [141, 174], phase contrast [13, 14], or Hoffman modulation contrast [175] microscopy. These methods generate contrast exploiting the local variations in refractive index across the cell. As a result, these technologies do not require fluorescence tagging and are relatively harmless. However, the relationship between the intensity map generated by these methods and the properties of the cell (e.g., thickness, mass) are only qualitative. Recently, QPI has been applied to imaging sperm cells as well [46, 176-178]. Particularly, several studies used QPI for measuring sperm motility [48, 179, 180].

Here, we show that using PICS allows us to identify subcellular compartments of unlabeled bovine spermatozoa, which can assist to produce intrinsic markers for reproductive outcomes. Because the QPI modules can be attached to existing microscopes, we anticipate that our approach will be adopted broadly.

To analyze microscope slides of bovine spermatozoa, we developed a deep learning system to label the pixels in the image as "head," "midpiece," "tail," or "background." The challenges for developing such a system are twofold. First, the system must be trained on annotated images that are labor-intensive to generate and necessarily include bias from the individual annotators. To that end, we developed a "bootstrapping" image segmentation approach that ameliorates these concerns by annotating a subset of images that are then used to train the initial classification system. The results of this initial classification form a larger set of training images that can be

quickly corrected for coarse defects and used to re-train the classification system. This approach produces a larger training set in a shorter period than finely annotating the entire training corpus.

The second challenge is to develop an efficient classification system. We followed the practices described in Section 3.3 and utilized the U-Net architecture. We trained two different models with 30 million parameters (Fig. 9A) and 1.9 million parameters, respectively. Both networks achieved over 0.8 F-1 score [181]. We then used the network to annotate the sperm cells across all slides, resulting in a semantic map for every SLIM image. Additionally, we used connected coordinate analysis to generate instance segmentation which separates individual sperm cells, enabling us to group the labels on a per-cell basis [182]. This step also removes sperm cells that are stuck together. The U-Net architecture is presented in Fig. 9A, and the complete workflow is shown in Fig. 9B.
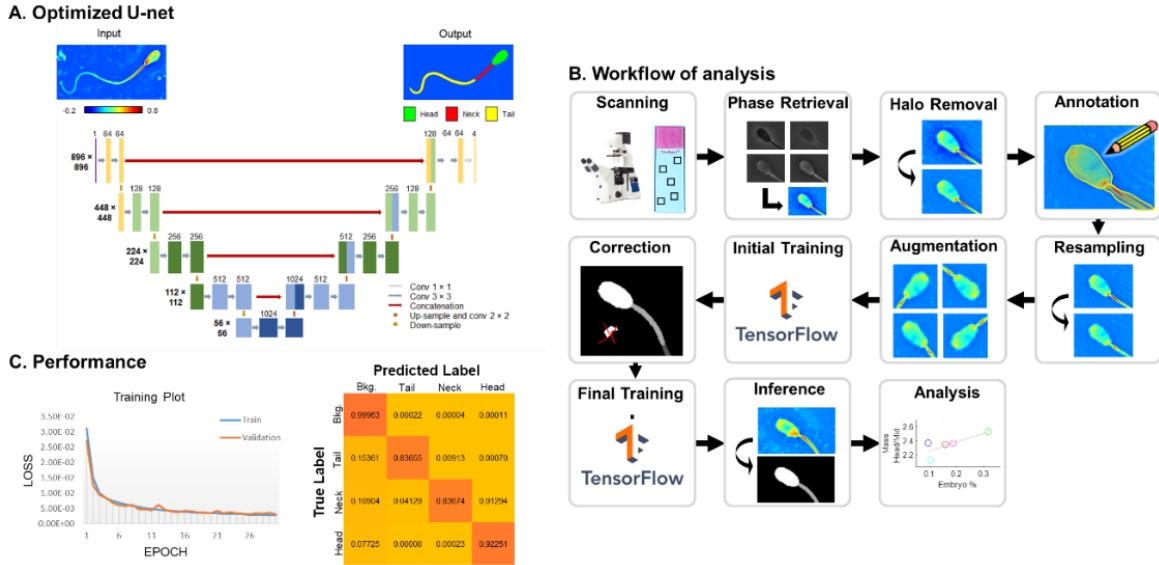
Figure 9. Reproductive Outcome Prediction Using PICS. (a) Semantic segmentation converts phase maps into a segmentation mask corresponding to the head, neck, and tail. The U-Net architecture performs well on our data, as it contains a large receptive field, well suited for the rich, broadband images typically found in microscopy. (b) Workflow for training a deep convolutional neural network on quantitative phase images and inferring the semantic segmentation. For each slide we performed z-stacks, selecting the fields of view with intact sperm cells. We recover the phase from the four intensity images and perform halo removal to account for the partially coherent illumination. Next, we use ImageJ to manually segment the cells into the head, neck, and tail. We down-sample the images to match the optical resolution and perform data augmentation by rotation and flipping. Training is performed using a TensorFlow back end. To boost the performance of our network, we correct for grossly defective segmentation using the Image Segmented App (part of MATLAB). This step is substantially faster than manually annotating every cell. A final training round is then performed using all data. By evaluating the network (inference) on all images, we obtain the segmentation results for all the cells, which are then used to determine the relationship between the dry mass of cellular ultrastructure and ART success rates. (c) Performance of the neural network in terms of the loss plot and confusion matrix. Adapted with permission from Ref [83].

The results in terms of percentages of zygotes cleaved and ready-to-transfer blastocysts produced are summarized in Fig. 10a. Statistically significant correlations between dry ratios and fertility outcomes are shown in bold. The graphs in Figs. 10b-c show these findings in more detail. Essentially, cleavage outcomes correlate negatively with head-to-tail and midpiece-to-tail dry mass ratios, but not statistically significantly for head-to-midpiece ratios. These results suggest that a long sperm tail is beneficial. However, when we evaluate the embryo blastocyst development rate, it appears that a large head-to-midpiece value is desirable, while the other two ratios are only weakly correlated. This result appears to indicate that a denser head promotes blastocyst

development. Note that this subgroup of spermatozoa that are associated with the embryo

blastocyst development rate has, with a high probability, larger tails (Fig. 10b).
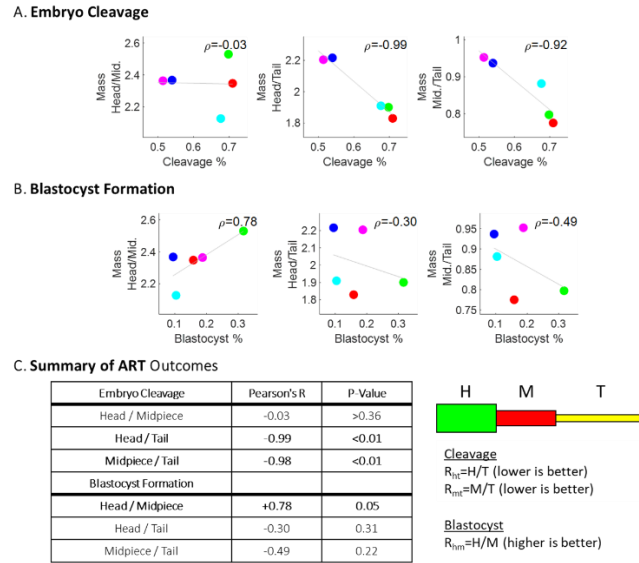
Figure 10. Summary of Outcomes. (a and b) Cleavage is strongly favored by a more massive tail (a), while blastocyst development is favored by a heavier head (b). (c) Summary across the five bulls for cleavage and blastocyst rates. H, head; Mid, midpiece; R_{hm}, head-to-midpiece ratio; R_{ht}, head-to-tail ratio; R_{mt}, midpiece-to-tail ratio; T, tail. Reprinted with permission from Ref [83].

We envision that our PICS-based system can be applied to individual sperm selection

which is performed on chemically slowed cells [183] or as a slide cytometer capable of

automatically assessing sperm sample quality. Since deploying the deep learning inference is

straight-forward, our methodology can likely be embraced at a large scale. Thus, our technology

may provide a solution for sperm classification and sorting in real-time, as well as provided

valuable insight into the relationships between cellular ultra-structure and fertility.

4. Computational Interference Microscopy

The figures of merits for QPI systems are discussed in Section 2.1. Usually off-axis methods provide fast acquisition rate, while white-light methods yield high spatial phase stability and thus less speckle noise. An ideal QPI method, taking the best from both worlds, would be able to provide the low noise, high resolution associated with phase shifting interferometry and single-shot performance associated with off-axis geometries.

As discussed in Section 1.2, deep learning has already been applied to enhance imaging systems. Inspired by previous works [184], we presented in this chapter Computation Interference Microscopy (CIM) [97], a QPI method with the ideal performance mentioned above, achieved by using deep learning to produce an image-to-image translation from single shot noisy data to phase-shifting, low-noise images, on which the network was *a priori* trained.

4.1 Methods

Similar to the PICS workflow explained in Chapter 3, the development of CIM can be broken into three major steps: acquiring SLIM and DPM image pairs for training, developing the deep learning algorithm, and applying the optimized model into the acquisition software. In this section, we explained the methods for all three steps.

4.1.1 Data Acquisition

In order to acquire training data necessary to produce SLIM-quality images in a single-shot, we developed a combined SLIM-DPM system, which generates both images from the same field of view (Figure 11). The DPM and SLIM modules were placed at the two side ports of a commercial inverted microscope (Axio Observer Z1, Zeiss). A coupled fiber green laser ($\lambda = 532\ nm$) was used as illumination for DPM, with the condenser aperture closed to minimum. A collimated LED source ($\lambda = 623\ nm$, 20 nm bandwidth) was used as illumination for SLIM

(CellVista SLIM Pro, Phi Optics, Inc.), with the conventional ring illumination associated with phase contrast microscopy. Using 20×/0.4 NA objective, the magnified image is replicated to either port by using a switch.
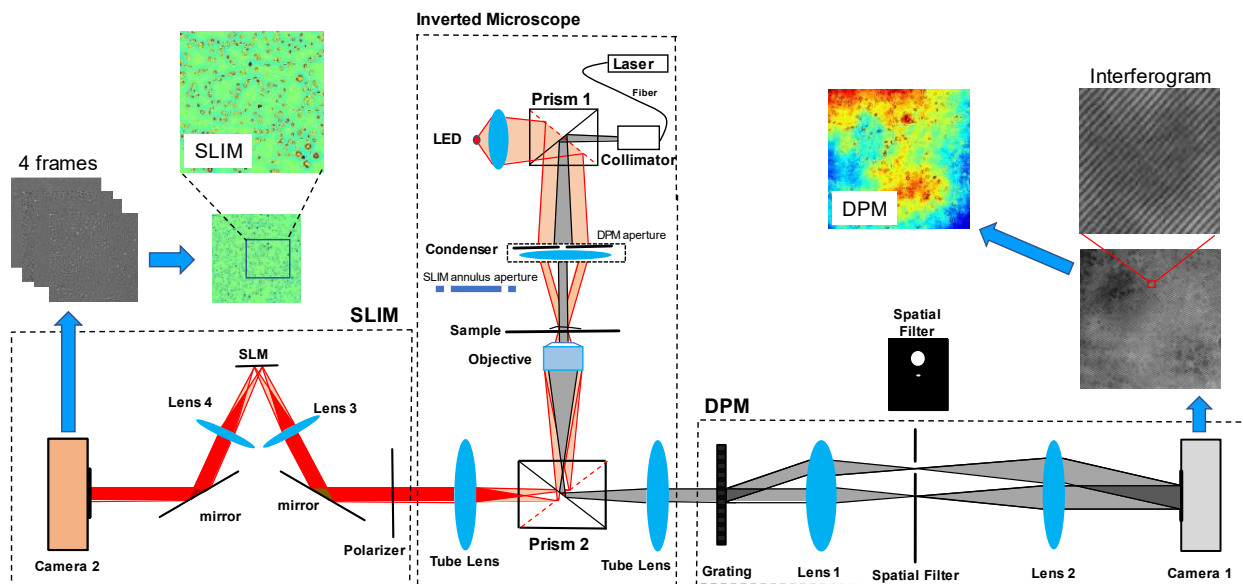
Figure 11. Schematic of the Imaging Setup. The system is built around an inverted microscope. We are using a 20×/0.4NA objective. The two side ports connect to the DPM (right) and SLIM (left) modules. Thus, we obtain SLIM and DPM images on the same field of view. The focal length of lenses 1 and 2 are 100 mm and 200 mm, respectively. Lenses 3 and 4 have the same focal length. When switching between DPM and SLIM, Prisms 1 and 2 are switched to different positions and the condenser is set to PH1 set. Due to the magnification of the 4*f* system in DPM, a registration is needed to match the DPM and SLIM images. Reprinted with permission from [97].

4.1.2 Deep Learning Development

We formulated the problem as an image-to-image translation problem [89], where the deep neural network takes in a DPM image as input and predicts a new image that is close to a SLIM image of the same field of view. Following the practices outlined in Chapter 3, we built our deep learning model based on the U-Net architecture. We first added Batch Normalization layers between convolution and activation layers to stabilize the learning process. We also added in a residual connection after every two convolution operations (on the same field of view) for faster convergence and better performance. The model has a symmetric layout and consists of three major parts: an encoder path, a bottleneck and a decoder path. The encoder path captures

34

contextual information in the image. It consists of 4 stages of convolutional and non-linear activation operations with residual connection. Each stage was followed by a 2×2 downsampling operation. The decoder path is almost symmetric to the encoder path, except that it has upsampling operations to combine low-resolution and high-resolution information and enables localization. The convolution kernel size within the network was set to 3×3 except for those used in residual connection, which was set to 1×1. The number of kernels in each stage were set to 16, 32, 64, and 128 respectively. Thus, our model had only 3.3 million trainable parameters. Based on the training results, it was apparent that this model was already complex enough to approximate the transform from DPM images to SLIM images. We picked the mean-squared error as our loss function and used the Adam optimizer [185] with the default exponential decay rate for both moment estimates (0.9 and 0.999, respectively). We used peak signal-to-noise ratio (PSNR), Pearson correlation coefficient, and structural similarity index (SSIM) to measure the performance of our network. All the input images (DPM and SLIM) were scaled from $[-\pi, \pi]$ to $[0,1]$. We trained the model from scratch with a learning rate of 6e-5 for 1,000 epochs. The batch size was set to 4 during training. The mean squared loss value on both the training and the validation dataset was plotted after each epoch. To add more variation during the training process, we applied random cropping to each training image. A 400×400 crop was selected randomly from each original 1536 x 1536 image and fed into the model during one epoch (see Chapter 3). Since U-Net is fully convolutional, it can pick up features on these smaller crops and apply them later onto the larger images. This random cropping has two main advantages. First, it served as a form of data augmentation, contributing to better generalizability. Second, it reduced the training time and GPU memory requirement. The model was implemented using TensorFlow

[162] and the training was performed on a GTX 1070 GPU with 8GB memory. The training took approximately 21 hours.

4.1.3 Deep Learning Deployment

We followed the practices outlined in Section 3.2 to incorporate the trained model into our acquisition software. First, we saved all the trained weights (convolution kernels and batch normalization parameters) into a single HDF5 [161] file. Then we constructed the same network architecture within our acquisition software using the Nvidia TensorRT API in C++. Due to the mismatch between weight formats in TensorFlow and TensorRT, the weights were first transposed and then loaded into the network architecture in C++. Once the network was built, TensorRT optimized the inference procedure by enumerating different configuration of kernels. This optimization was necessary because the optimal configuration for inference differ on from hardware to hardware. Thus, we overlapped the model optimization with the software initialization by utilizing multi-threading in C++.

4.2 Results

Figure 12 illustrates the DPM input data (left column), SLIM ground truth (middle), and the resulting CIM (right). Visually, the U-Net is able to reduce the overall noise of the DPM input and produce a remarkably similar image to the SLIM ground truth. In order to quantify the performance of the neural network, we computed PSNR, Pearson correlation, and SSIM between the ground truth and the prediction. The mean-squared loss value on the training dataset and the validation dataset after each epoch is plotted in Figure 12. The model checkpoint with lowest loss value on the validation dataset was selected as our end model for evaluation and deployment. Figure 12 also shows the result of the average PSNR, Pearson correlation and structural similarity index measure (SSIM) calculated on the training, validation, and test

datasets. The results are consistent among all three datasets, indicating that the model

generalized well on the unseen test dataset. Figure 13 illustrates the images with lowest, average

and highest Pearson correlation. The profile of RBC at exact same position were plot. The result

indicates that all the structure are properly calculated, while the CIM image with higher Pearson

correlation have a closer profile.
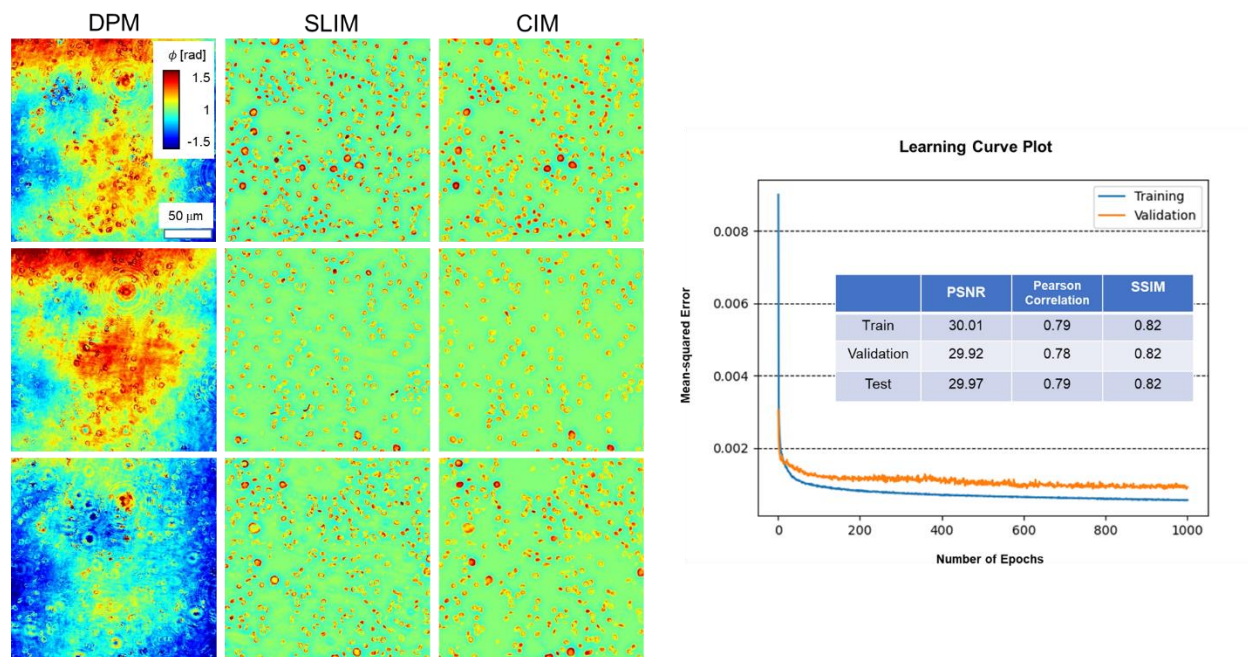
Figure 12. CIM Development. DPM input data (left column), SLIM ground truth data (center) and the U-net inference (right). All images share the same calibration and scale bar. As can be seen, the neural network correctly infers SLIM images from the DPM input, with drastically reduced noise levels. The learning curve plot is shown on the right. As can be seen, the model's performance remained stable among all three datasets. Reprinted with permission from [97].

To boost the usability of CIM, we integrated the inference algorithm into the real-time

acquisition software for DPM (wDPM CellVista Pro, Phi Optics, Inc.). Figure 14 shows the user

interface, with the DPM image being reconstructed and used as input for inference. Ref [97]

includes a video demonstration. The conversion from the noisy DPM images to CIM takes place

at a push of a button. Note that translating the stage does not affect the quality of the inference,

which works very well for both red and white blood cells. Thus, we envision that CIM can be

readily used for automating large field of view and multi-well plate scanning.

37
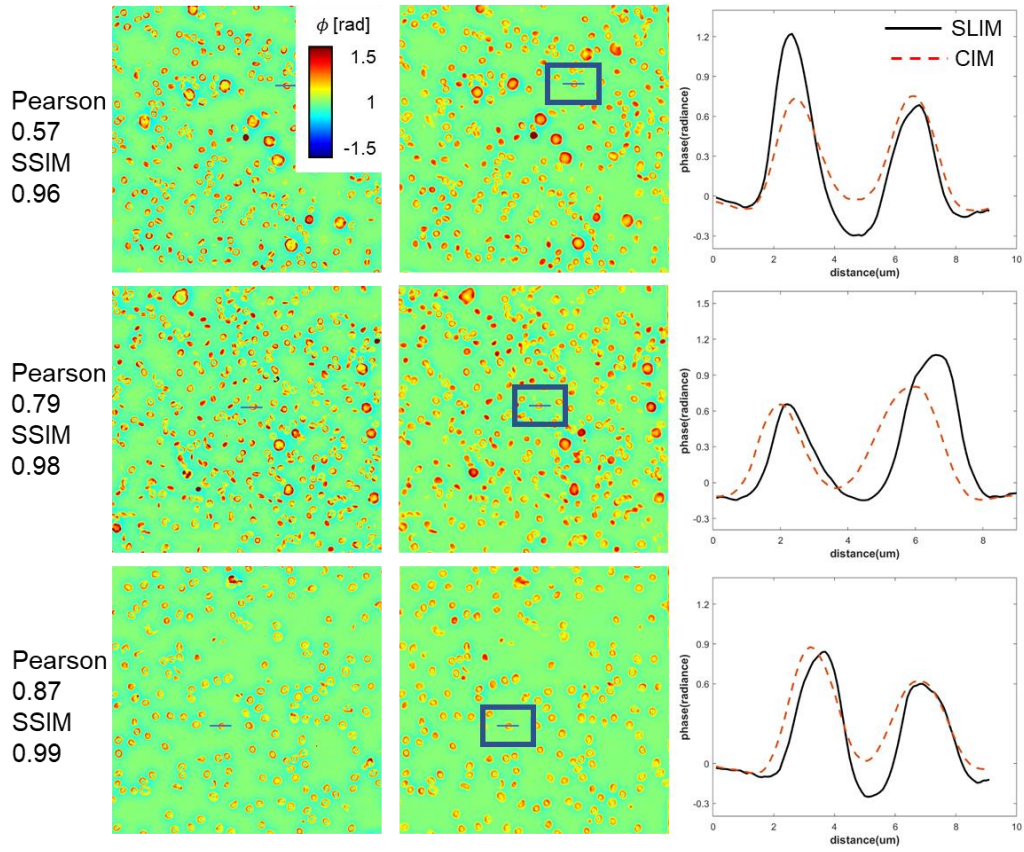
Figure 13. CIM Performance. Comparison of the lowest, average and highest Pearson correlation output images. The data were chosen from the test set. We plot the profile of chosen RBC at the exact same pixel position. All the structure were properly calculated, while the CIM image with higher Pearson correlation had a closer profile compared to SLIM image. Reprinted with permission from [97].

To validate the performance of our method on unseen data, we collected blood from a healthy volunteer, diluted one drop of blood with 10 ml Phosphate-buffered saline. No effect was devoted to stabilizing the smear, such that we can test the ability of CIM to operate on highly dynamic samples. Clearly CIM performs very well and even reveals minute membrane fluctuation in individual red blood cells. The area of cell overlapping sometimes display lower phase values than expected, but this appears to be an optical, rather than computational artifact, as it is also present in Fig. 4 (SLIM column). These data highlight the capability of CIM to run under flow conditions, for applications such as flow cytometry. Figure 15 shows 4 sequential frames from the time lapse in Visualization 2 of Ref [97], taken 100 ms apart, with 2 ms

38

exposure each. The cells selected in the rectangular boxes moved very fast, as can be visualized in the movie and these snapshots. These results prove that the CIM system can provide single-shot, high speed measurements, as allowed by DPM, while the output has the high quality of SLIM images.
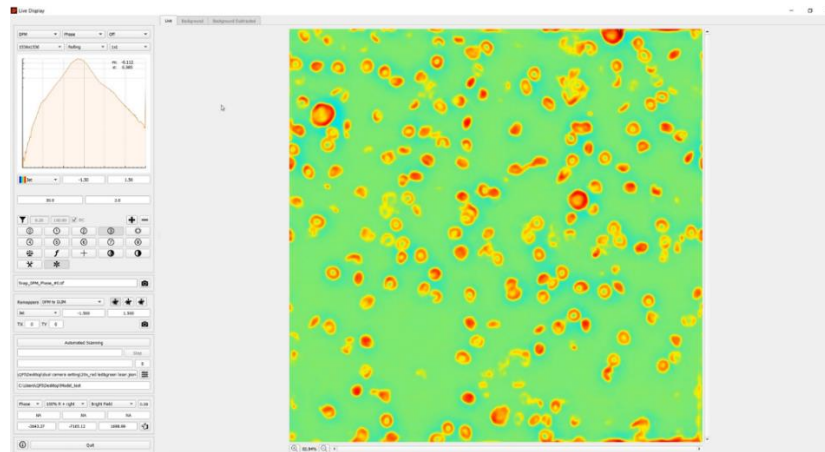
Figure 14. Live Imaging Interface. The image shows the graphic user interface and a snapshot of CIM operation in real-time. Reprinted with permission from [97].
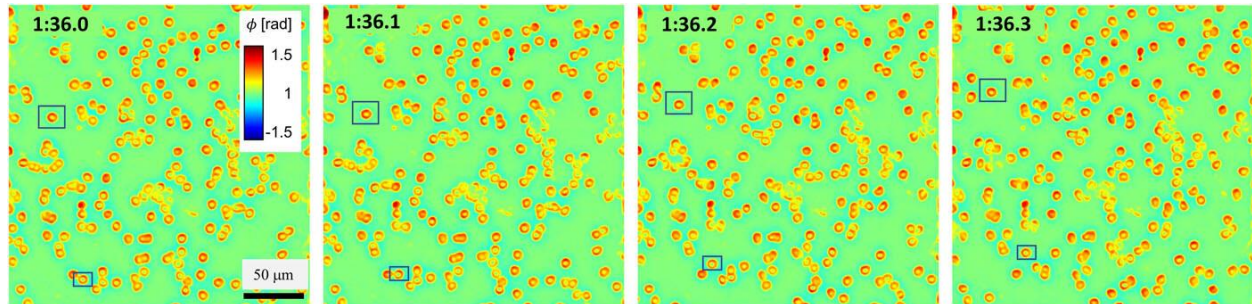
Figure 15. Dynamic Imaging of Blood Cells. Dynamic imaging of blood cells with snapshots at different moments in time, 100 ms apart, as indicated. The scale bar and color bar are the same for all the frames. In these frames, one can see cells (e.g., those in the rectangular boxes) that flow very fast. However, the CIM inference is accurate and operates in real-time. Reprinted with permission from [97].

5. Cell Cycle Detection via PICS

Traditional methods for cell cycle stage classification rely heavily on fluorescence microscopy to monitor nuclear dynamics. These methods inevitably face the typical phototoxicity and photobleaching limitations of fluorescence imaging. In this chapter, we present a new label-free cell cycle detection workflow using the principle of PICS. The proposed method uses neural networks to extract cell cycle-dependent features from QPI measurements directly. Our results indicate that the new method attains 0.76, 0.76, and 0.60 F-1 scores in classifying live cells into G1, S, and G2/M stages, respectively. We also demonstrate that the proposed method can be applied to study single-cell dynamics within the cell cycle as well as cell population distribution across different stages of the cell cycle. We envision that the proposed method can become a nondestructive tool to analyze cell cycle progression in applications ranging from cell biology research to biopharma applications.

5.1 Motivation

The cell cycle [186] is a complex and ubiquitous process encompassing a series of ordered stages that can lead to mitosis and cellular division. It is involved in many biological events such as cell growth, organismal development, and diseases. Significantly, alteration in the cell cycle progression is one major mechanism that cells have developed to cope with DNA damage [187], which is central to both the cause and cure of cancer. Thus, understanding the cell cycle progression as part of cellular responses to DNA damage has emerged as an active field in cancer biology [188, 189].

Morphologically, the cell cycle can be divided into interphase and mitosis. The interphase can further be divided into three stages: G1, S, and G2 [186]. Since the cells are preparing for DNA synthesis and mitosis during G1 and G2 respectively, these two stages are also referred to as

the "gaps" of the cell cycle [190]. During the S stage, the cells are synthesizing DNA, with the chromosome count increasing from 2N to 4N.

Traditional approaches to distinguish different stages within the cell cycle rely on fluorescence microscopy [5] to monitor the activity of proteins that are involved in DNA replication and repair, e.g. proliferating cell nuclear antigen (PCNA) [191, 192]. Historically, a variety of signal processing techniques, including support vector machine (SVM) [193], intensity histogram and intensity surface curvature [194, 195], level-set segmentation [196], and k-nearest neighbor [197] have been applied to fluorescence intensity images to perform classification. In recent years, with the rapid development of parallel-computing capability [66, 162] and deep learning algorithms [89, 198, 199], convolutional neural networks have also been applied to fluorescence images of single cells for cell cycle tracking [200, 201]. Since all these methods are based on fluorescence microscopy, they inevitably face the associated limitations, including photobleaching, chemical, and phototoxicity, weak fluorescent signals that require large exposures, as well as nonspecific binding. These constraints limit the applicability of fluorescence imaging to studying live cell cultures over large temporal scales [202].

In this chapter we present a new methodology for label-free cell cycle detection that utilizes phase imaging with computational specificity (PICS) (see Ref [82-85] and Chapter 3). Our workflow combines spatial light interference microscopy (SLIM) (see Ref [108, 109] and Chapter 2), a highly sensitive QPI method, with recently developed deep learning network architecture E-U-Net [149, 203, 204]. We demonstrate on live cell cultures that the proposed method classifies cell cycle stages solely using SLIM images. The signals from the fluorescent ubiquitination-based cell cycle indicator (FUCCI) [148] were only used to generate ground truth annotations during the deep learning training stage. Unlike previous methods that perform single-cell classification based

41

on bright-field and dark-field images from flow cytometry [205] or phase images from ptychography [206], our method can classify all adherent cells in the field of view and perform longitudinal studies over many cell cycles. Evaluated on a test set consisting of 408 unseen SLIM images (over 10,000 HeLa cells), our method achieves over 0.75 F-1 scores for both the G1 and S stage, and an 0.6 F-1 score for the G2/M stage. We also show that our method allows for the investigation of single cell area and dry mass change within the cell cycle as well as the cell area and dry mass distribution of cell populations in different cell cycle stages. We envision that our proposed method can be extended to different cell lines and other QPI imaging modalities for high through-put and nondestructive cell cycle analysis, thus, eliminating the need for cell synchronization [207, 208].

5.2 Methods

We presented, in this section, the sample preparation procedure, the imaging experiment setup, the deep learning model development, and the evaluation and application of the proposed cell cycle stage classification method.

5.2.1 Cell Preparation

HeLa/FUCCI(CA)2 [148] cells were acquired from RIKEN cell bank and kept frozen in liquid nitrogen tank. Prior to the experiments, we thawed and cultured cells into T75 flasks in Dulbecco's Modified Eagle Medium (DMEM with low glucose) containing 10% fetal bovine serum (FBS) and incubated in 37°C with 5% CO_2. When the cell reached 70% confluency, the flask was washed with phosphate-buffered saline (PBS) and trypsinized with 4 mL of 0.25% (w/v) Trypsin EDTA for four minutes. When the cells started to detach, they were suspended in 4 mL of DMEM and passaged onto a glass-bottom six-well plate. HeLa cells were then imaged after two days of growth.

5.2.2 SLIM Imaging

The SLIM system architecture is shown in Fig. 16a, and more details can be found in Section 2.3. We attached a SLIM module (CellVista SLIM Pro; Phi Optics) to the output port of a phase contrast microscope. Inside the SLIM module, the spatial light modulator matched to the back focal plane of the objective controlled the phase delay between the incident field and the reference field. We recorded four intensity images at phase shifts of 0, $\pi/2$, π, and $3\pi/2$ and reconstructed the quantitative phase map of the sample. We measured both the SLIM signal and the fluorescence signal with a 10×/0.3NA objective. The camera we used was Andor Zyla with a pixel size of 6.5 µm. The exposure time for SLIM channel and fluorescence channel was set to 25 ms and 500 ms, respectively.
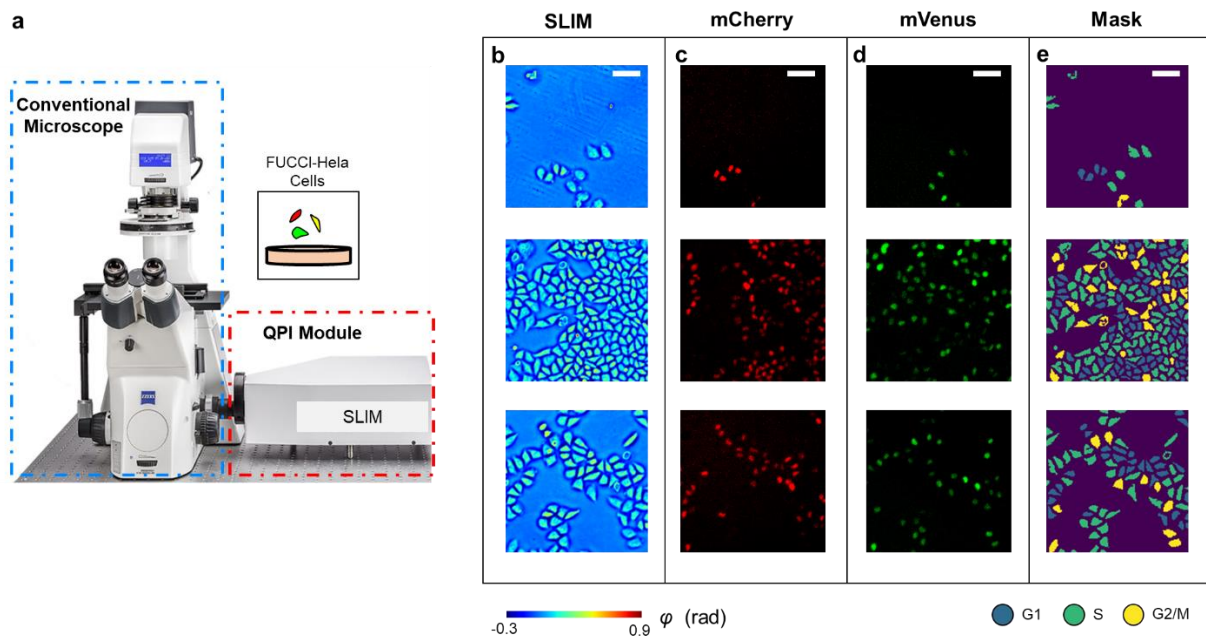
Figure 16. Schematic of the Imaging System. (a) The SLIM module was connected to the side port of an existing phase contrast microscope. This setup allows us to take co-localized SLIM images and fluorescence images by switching between transmission and reflection illumination. (b) Measurements of HeLa cells. (c) mCherry fluorescence signals. (d) mVenus fluorescence signals. (e) Cell cycle phase masks generated by using adaptive thresholding to combine information from all three channels. Scale bar is 100 µm.

5.2.3 Cellular Dry Mass Computation

As the refractive index is linearly proportional to cell density [15, 16], independent of composition, QPI methods can be used to measure the non-aqueous content (dry mass) of the cellular culture [28]. We recovered the dry mass density as

$$m(x, y) = \frac{\lambda}{2\pi\gamma} \phi(x, y) \tag{5.1}$$

using the same procedure outlined in previous works [15, 28, 33, 83]. $\lambda = 550 \, nm$ is the central wavelength; $\gamma = 0.2 \, ml/g$ is the specific refraction increment, corresponding to the average of reported values [15, 209]; and $\phi(x, y)$ is the measured phase. Equation (5.1) provides the dry mass density at each pixel, and we integrated over the region of interest to get the cellular dry mass. In Equation (5.2), M_C denotes the cellular dry mass associated with cell mask C. To retrieve this quantity, for each pixel within the mask, we multiply the dry mass density with the unit area ΔA, which is determined by the camera pixel size as well as the magnification used.

$$M_C = \sum_{(x,y)\in C} m(x, y) \cdot \Delta A \tag{5.2}$$

5.2.4 Ground Truth Cell Cycle Mask Generation

To prepare the ground truth cell cycle masks for training the deep learning models, we combined information from the SLIM channel and the fluorescence channels (Fig. 17a) by applying adaptive thresholding (Fig. 17b). All the code was implemented in Python, using the scikit-image library [210]. We first applied the adaptive thresholding algorithm on the SLIM images to generate accurate cell body masks. Then we applied the algorithm on the mCherry fluorescence images and mVenus fluorescence images to get the nuclei masks that indicate the presence of the fluorescence signals. The window size used in the adaptive thresholding algorithm was tuned by visually inspected the correlation between the generated mask and the SLIM image. We took the

44

intersection between the three sets of masks. Following the FUCCI color readout detailed in [148], a presence of mCherry signal alone indicates the cell is in G1 stage and a presence of mVenus signal alone indicates the cell is in S stage. The overlapping of both signals indicates the cell is in G2 or M stage. Since the cell mask is always larger than the nuclei mask, we filled in the entire cell area with the corresponding label. We handled the case of no fluorescence signal by automatically labeling them as S because both fluorescence channels yield low-intensity signals only at the start of the S phase [148]. Before using the mask for analysis, we also performed traditional computer vision operations, e.g., hole filling. on the generated masks to ensure the accuracy of computed dry mass and cell area (Fig. 17c).
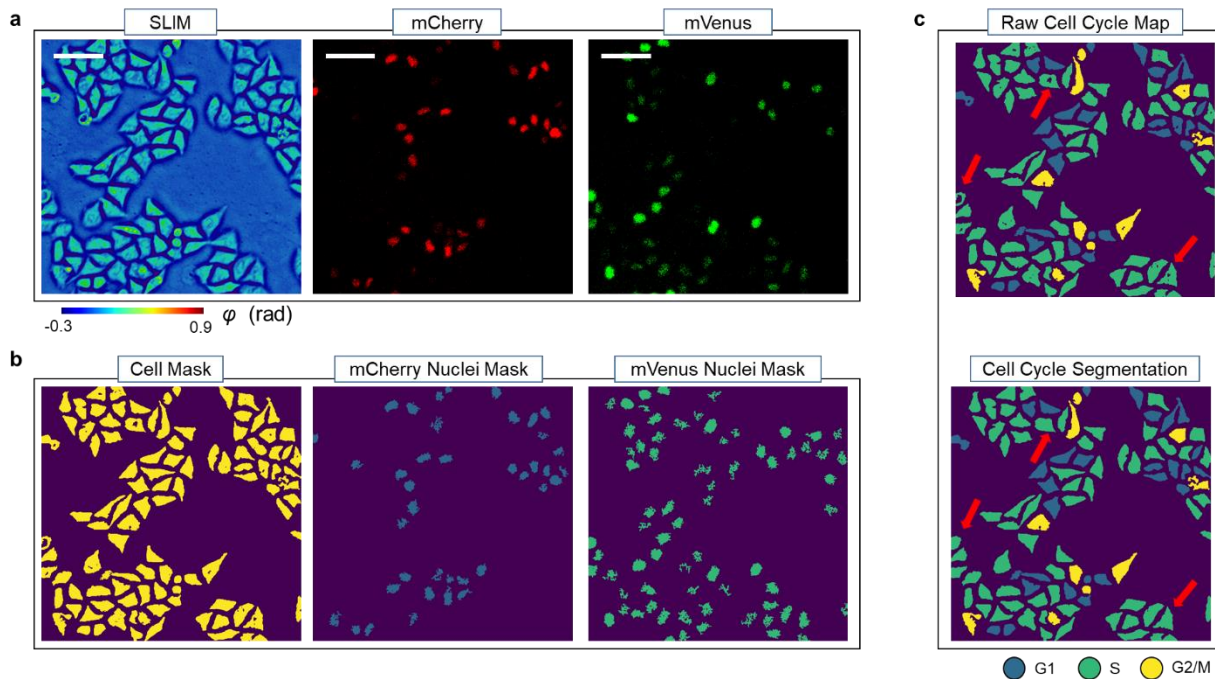
Figure 17. Ground Truth Mask Generation Workflow. (a) Images from the SLIM channel (left), mCherry channel (middle) and the mVenus channel (right). (b) Preliminary masks generated from the SLIM and fluorescence images using adaptive thresholding. (c) Combing three masks in b. Holes in cell masks were removed during analysis to avoid errors in cell dry mass and area. Scale bar is 100 μm.

5.2.5 Deep Learning Model Development

We used the E-U-Net architecture [84, 204] to develop the deep learning model that can assign a cell cycle phase label to each pixel. The E-U-Net upgraded the classic U-Net [149] architecture by

swapping its encoder component with a pre-trained EfficientNet [203]. Compared to previously reported transfer-learning strategies [211, 212], e.g. utilizing a pre-trained ResNet [152] for the encoder part, we believe the E-U-Net architecture is superior since the pre-trained EfficientNet attains higher performance on the benchmark dataset [73] while remaining compact due to the compound scaling strategy [203].

The EfficientNet backbone we ended up using for this project was EfficientNet-B4 (Fig. 18a). The entire E-U-Net-B4 model contains around 25 million trainable parameters, which is smaller compared to the number of parameters from the stock U-Net [83, 85, 149] and other variations [213, 214]. We trained the network with 2046 image pairs in the training dataset and 408 image pairs in the validation dataset. Each image contains 736×736 pixels. The model was optimized using an Adam optimizer [185] with default parameters against the sum of the DICE loss [215] and the categorical focal loss [216]. The DICE loss was designed to maximize the dice coefficient D (Equation (5.3)) between the ground truth label (g_i) and prediction label (p_i) at each pixel. It has been shown in previous works that DICE loss can help tackle class imbalance in the dataset [217, 218]. Besides DICE loss, we also utilized the categorical focal loss $FL(p_t)$ (Equation (5.4)). The categorical focal loss extended the cross-entropy loss by adding a modulating factor $(1 - p_t)^\gamma$. It helped the model to focus more on wrong inferences by preventing easily classified pixels dominating the gradient. We tuned the ratio between these two loss values and launched multiple training sessions. In the end we found the model trained against an equally weighted DICE loss and categorical focal loss gave the best results.

$$D = \frac{2 \sum_i^N p_i g_i}{\left(\sum_i^N p_i^2 + \sum_i^N g_i^2\right)} \tag{5.3}$$

$$FL(p_t) = -(1 - p_t)^\gamma \log(p_t) \tag{5.4}$$

The model was trained for 120 epochs, taking over 18 hours on an Nvidia V-100 GPU. For learning rate scheduling, we followed previous works [219-221] and implemented learning rate warmup and cosine learning rate decay. During the first five epochs of training, the learning rate will increase linearly from 0 to 4×10^{-3}. After that, we decreased the learning rate at each epoch following the cosine function. Based on our experiments, we ended up relaxing the learning rate decay such that the learning rate in the final epoch will be half of the initial learning rate instead of zero [220]. We plotted the model's loss value on both the training dataset and the validation dataset after each epoch (Fig. 18b) and picked the model checkpoint with the lowest validation loss as our final model to avoid overfitting. All the deep learning code was implemented using Python 3.8 and TensorFlow 2.3.
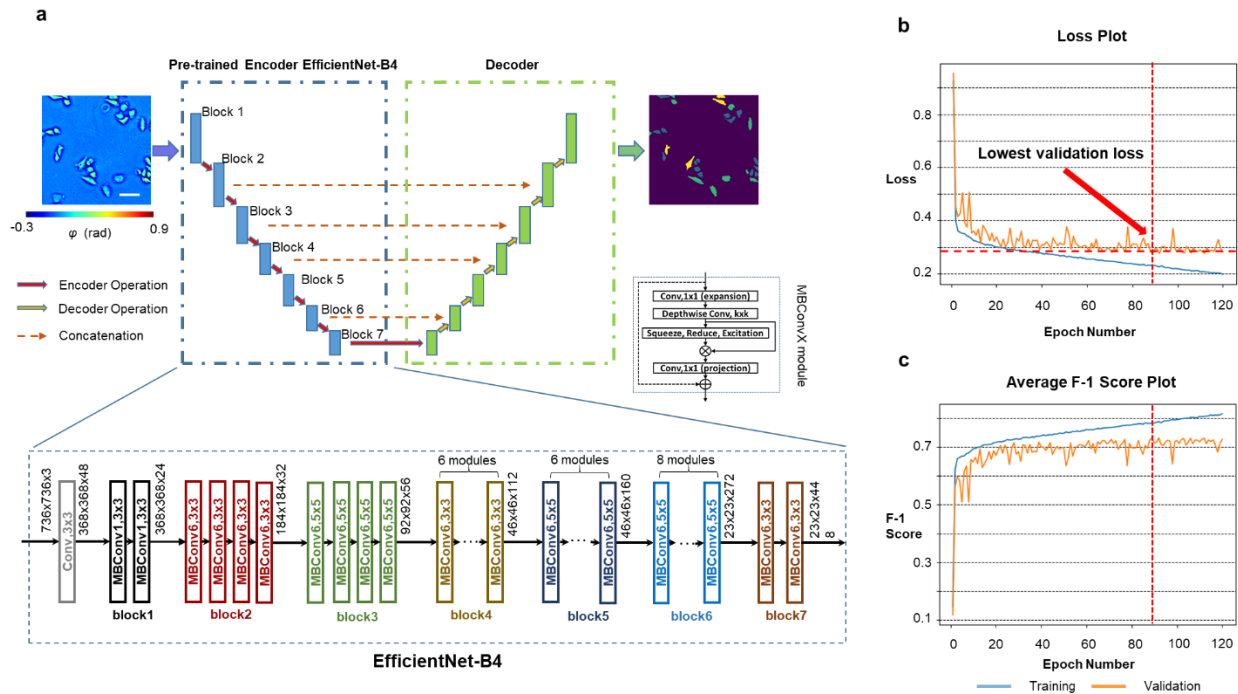
Figure 18. PICS Training Procedure. (a) We used a network architecture called the E-U-Net that replaces the encoder part of a standard U-Net with the pre-trained EfficientNet-B4. Within the encoder path, the input images were downsampled 5 times through 7 blocks of encoder operations. Each encoder operation consists of multiple MBConvX modules that consist of convolutional layers, squeeze and excitation, and residual connections. The decoder path consists of concatenation, convolution and upsampling operations. (b) The model loss values on the training dataset

and the validation dataset after each epoch. We picked the model checkpoint with the lowest validation loss as our final model and used it for all analysis. (c) The model's average F-1 score on the training dataset and the validation dataset after each epoch.

5.2.6 Post-processing for Cellular Level Evaluation

We evaluated the performance of our trained E-U-Net on an unseen test dataset and reported the precision, recall, and F-1 score for each category: G1, S, G2/M, and background, respectively (Fig. 19). The pixel-wise confusion matrix indicated our model achieved high performance in segmenting the cell bodies from the background. However, since this pixel-wise evaluation overlooked the biologically relevant instance, i.e., the number of cells in each cell cycle stage, we performed an extra step of post-processing to evaluate that.

Prediction / True Label	Background	G1	S	G2/M
Background (n = 204,426,215)	99.75%	0.03%	0.17%	0.05%
G1 (n = 5,149,858)	1.50%	70.27%	26.21%	2.01%
S (n = 8,687,486)	1.88%	10.14%	75.12%	12.87%
G2/M (n = 2,748,409)	1.37%	6.42%	30.19%	62.02%
Precision	99.86%	76.34%	72.13%	56.13%
Recall	99.75%	70.27%	75.12%	62.02%
F1 Score	99.81%	73.18%	73.59%	58.93%

Figure 19. PICS Performance Evaluated at a Pixel Level.

We first performed connected-component analysis on the raw model predictions. Within each connected component, we applied a simple voting strategy where the majority label will take over the entire cell. Figures 20a-b illustrate this process. We believe enforcing particle-wise consistency, in this case, is justified because it is impossible for a single cell to have two cell cycle stages at the same time and that our model is highly accurate in segmenting cell bodies, with over 0.96 precision and recall (Fig. 19). We then computed the precision, recall, and F-1 score for each

category on the cellular-level. For each particle in the ground truth, we used its centroid (or the median coordinates if the centroid falls out of the cell body) to determine if the predicted label matches the ground truth. The cellular-wise metrics were reported in Fig. 21d.

Before using the post-processed prediction masks to compute the area and dry mass of each cell, we also performed hole-filling as we did for the ground truth masks to ensure the values are accurate (Fig. 20c).
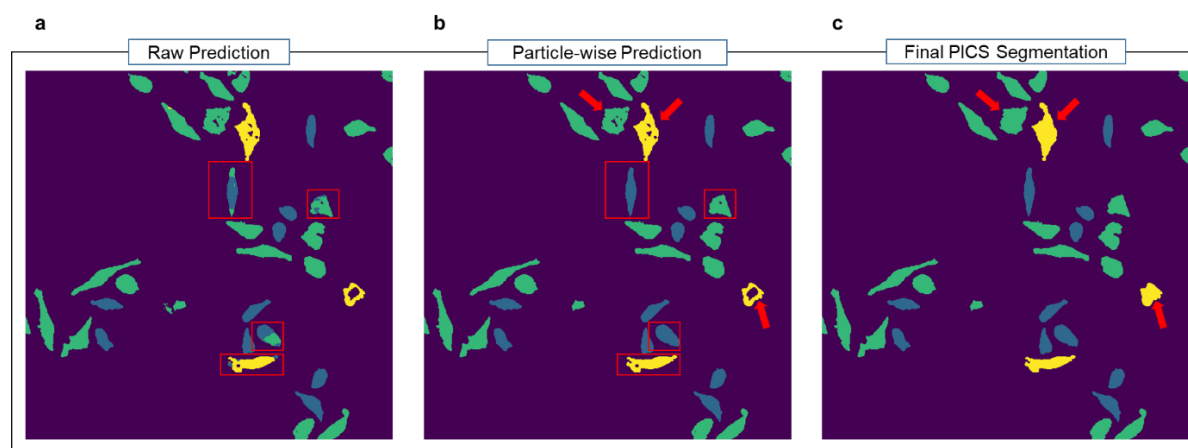
Figure 20. Post-processing Workflow. (a) Raw prediction from PICS. (b) Prediction map after enforcing particle consistency and removing small particles. A few examples were shown in the red rectangles. (c) Prediction map after filling in the holes in the masks. Masks at this stage were used for analysis.
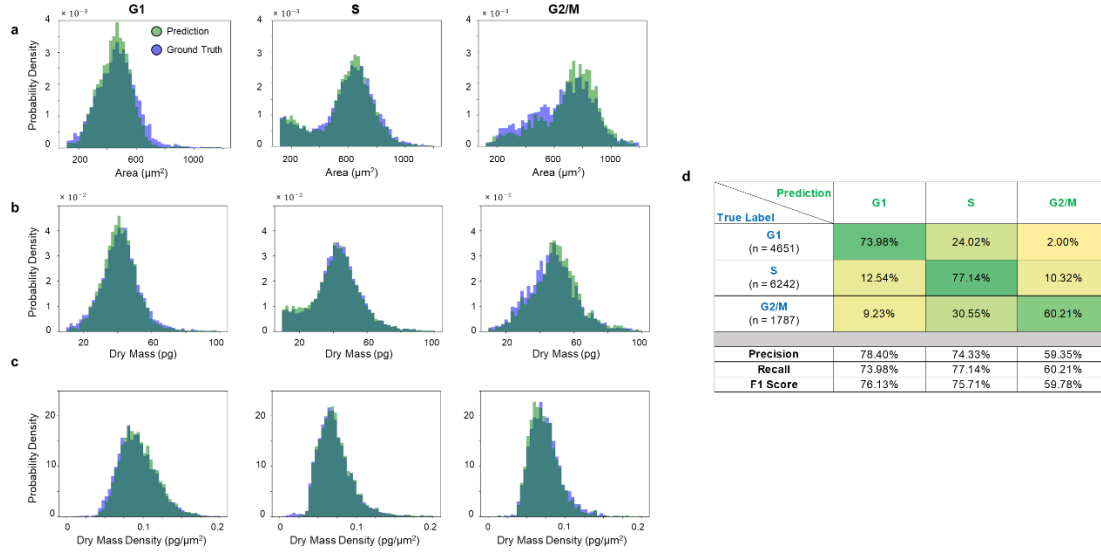
Figure 21. PICS Performance. (a) Cell area histograms for cells in G1, S, and G2/M, generated by the ground truth mask (in blue) and by PICS (in green). (b) Cell dry mass histograms for cells in G1, S, and G2/M, generated by the ground truth mask (in blue) and by PICS (in green). (c) Cell dry mass density histogram for cells in G1, S, and G2/M, generated by the ground truth mask (in blue) and by PICS (in green). (d) Confusion matrix for PICS inference on the test dataset.

5.3 Results

In this section, we first present both the raw performance of our model, and the cellular level performance after the post-processing step. Then we demonstrate the application of our method on both single cells and cell populations.

5.3.1 PICS Performance

After training the model, we evaluated its performance on 408 unseen SLIM images from the test dataset. The test dataset was selected from wells that are different from the ones used for network training and validation during the experiment. Figure 22a shows randomly selected images from the test dataset. Figures 22b-c show the corresponding ground truth cell cycle masks and the PICS cell cycle masks, respectively. It can be seen that the trained model was able to identify the cell body accurately.

50
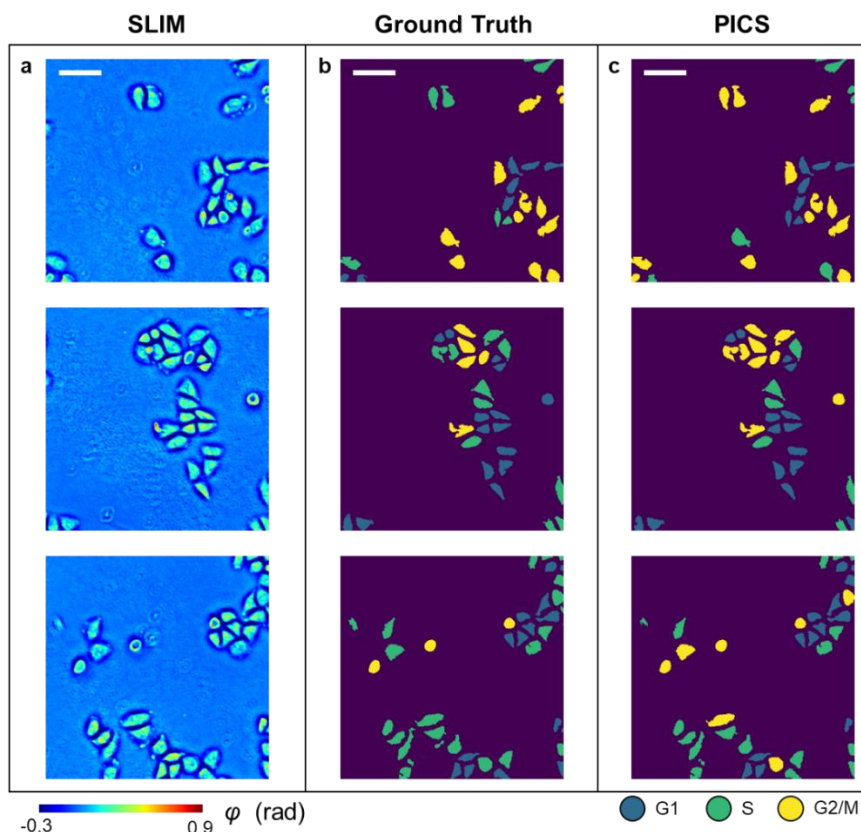
Figure 22. PICS Results on the Test Dataset. (a) SLIM images of Hela cells from the test dataset. (b) Ground truth cell cycle phase masks. (c) PICS-generated cell cycle phase masks. Scale bar is 100 μm.

We reported the raw performance of our PICS methods in Fig. 19, with pixel-wise precision, recall, and F1-score for each class. However, we noticed that these metrics did not reflect the performance in terms of the number of cells. Thus, we performed a post-processing step on the inferred masks to enforce particle-wise consistency, as detailed in Section 5.2.6. After this post-processing step, we evaluated the model's performance on the cellular level and produced the cell count-based results shown in Fig. 21. Figure 21a shows the histogram of cell body area for cells in different stages, derived from both the ground truth masks and the prediction masks. Figures 21b and 21c show similar histograms of cellular dry mass and dry mass density, respectively. The histograms indicated that there is a close overlap between the quantities derived from the ground truth masks and the prediction masks. We also reported the cellular-wise precision, recall, and F-

51

1 score for all three stages in Fig. 21d. Each entry is normalized with respect to the ground truth number of cells in that stage. Our deep learning model achieved over 0.75 F-1 scores for both the G1 stage and the S stage, and a 0.6 F-1 score for the G2/M stage.

5.3.2 PICS Application

The PICS method can be applied to track the cell cycle transition of single cells, nondestructively. Figure 5a shows the time-lapse SLIM measurements and PICS inference of HeLa cells. The time increment was roughly two hours between two measurements and the images at $t = 2, 6, 10,$ and 14 hours were displayed in Fig. 23a. Our deep learning model has not seen any of these SLIM images during training. The comparison between the SLIM images and the PICS inference showed that the deep learning model produced accurate cell body masks and assigned viable cell cycle stages. We showed in Fig. 23b-c the results of manually tracking two cells in this field of view across 16 hours and using the PICS cell cycle masks to compute their cellular area and dry mass. Figure 23b demonstrates the cellular area and dry mass change for the cell marked by the red rectangle. We observed an abrupt drop in both the area and dry mass around $t = 8$ hours, at which point the mother cell divides into daughter cells. The PICS cell cycle mask also captured this mitosis event as it progressed from the "G2/M" label to the "G1" label. We observed a similar drop in Fig. 23c after 14 hours due to mitosis marked by the orange rectangle. Figure 5c also shows that the cell continues growing before $t = 14$ hours and the PICS cell cycle mask progressed from the "S" label to the "G2/M" label correspondingly.
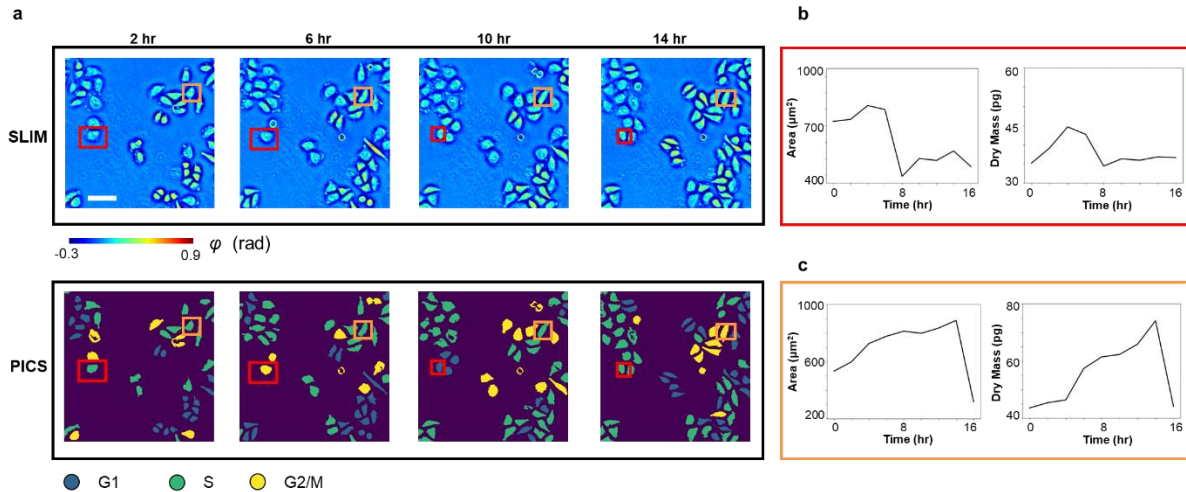
Figure 23. PICS on Time-lapse of FUCCI-Hela Cells. (a) SLIM images and PICS inference of cells measured at 2, 6, 10, and 14 hours. The time interval is roughly 2 hours. We manually tracked two cells (marked in red and orange). (b) Cell area and dry mass change of the cell in the red rectangle, across 16 hours. These values were obtained via PICS inferred masks. We can observe an abrupt drop in cell dry mass and area as the cell divides after around 8 hours. (c) Cell area and dry mass change of the cell in orange rectangle, across 16 hours. We can observe that the cell continues growing in the first 14 hours as it goes through G1, S, and G2 phase. It divides between hour 14 and hour 16, with an abrupt drop in its dry mass and cell area. Scale bar is 100 μm.

We also demonstrated that the PICS method can be used to study the statistical distribution of cells across different stages within interphase. The cell area distribution across G1, S, and G2/M was plotted in Fig. 24a and a clear shift between cellular area in these stages can be observed. We performed Welch's t-test on these 3 groups of data points. To avoid the impact on p-value due to the large sample size, we randomly sampled 20% of all data points from each group and performed the t-test on these subsets instead. After sampling, we have 884 cells in G1, 1345 cells in S, and 373 cells in G2/M. The p-values are less than 10^{-3}, indicating statistical significance. The same analysis was performed on the cell dry mass and cell dry mass density, as shown in Figs. 24b-c. We observed a clear distinction between cell dry mass in S and G2/M as well as between cell dry mass density in G1 and S. These results agree with the general knowledge that cells are metabolically active and grow during G1 and G2. During S, the cells remain metabolically inactive and replicate their DNA. Since the DNA dry mass only accounts for a very small factor of the total cell dry mass [222], the distinction between G1 cell dry mass and S cell dry mass is less obvious

than the distinction between S cell dry mass and G2/M cell dry mass. We also noted that our

observation on the cell dry mass density distribution agrees with previous findings [32].
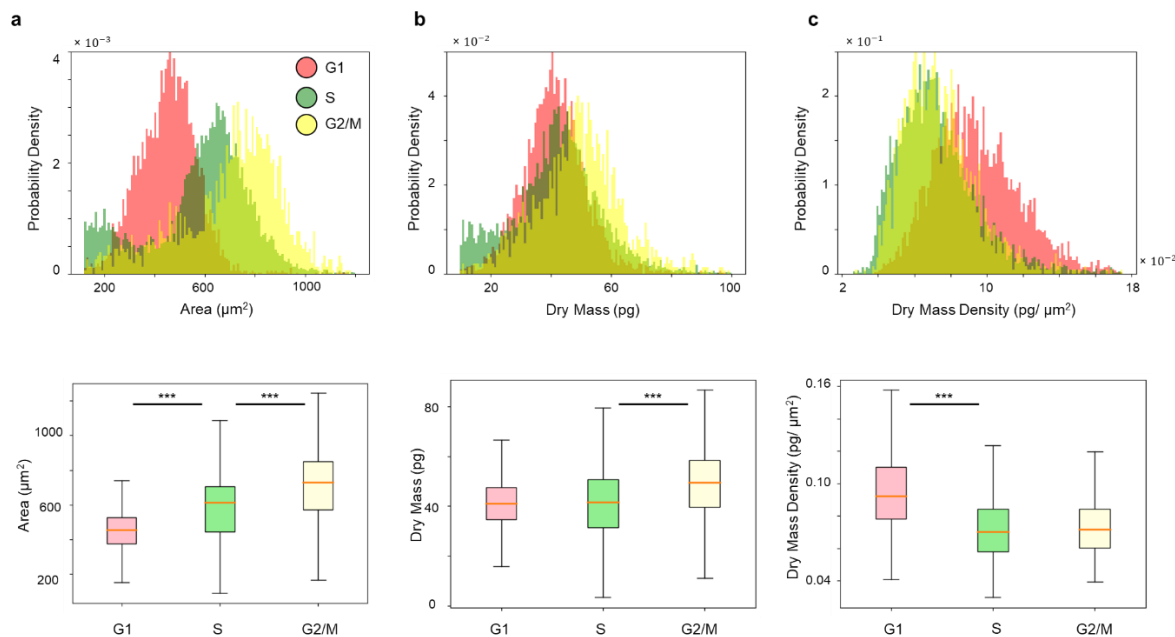
Figure 24. Statistical Analysis from PICS Inference on the Test Dataset. (a) Histogram and box plot of cell area. The p-value returned from Welch's t-test indicated statistical significance. (b) Histogram and box plot of cell dry mass. The p-value returned from Welch's t-test indicated statistical significance. (c) Histogram and box plot of cell dry mass density. The p-value returned from Welch's t-test indicated statistical significance comparing cells in G1 and S. The box plot and Welch's t-test are computed on 20% of all data points in G1, S, and G2/M, randomly sampled. The sample size is 884 for G1, 1345 for S, and 373 for G2/M. Outliers are omitted from the box plot. (*** $p < 0.001$).

5.4 Discussion

We proposed a PICS-based cell cycle stage classification workflow for fast, label-free cell cycle

analysis on adherent HeLa cell cultures. Our new method utilizes trained deep neural networks to

infer an accurate cell cycle mask from a single SLIM image. The method can be applied to study

single-cell dynamics within the cell cycle as well as compare the cellular parameter distributions

between cells in different cell cycle phases.

Compared to many existing methods of cell cycle detection [193-197, 200, 201, 205, 206],

we believe that our method has three main advantages. First, our method uses a SLIM module,

which can be installed as an add-on component to a conventional phase contrast microscope. The

imaging cost and setup complexity are much lower compared to previous methods using flow

cytometry [205], while the user experience remains the same as using a commercial microscope. Significantly, due to the seamless integration with the fluorescence channel on the same field of view, the instrument can collect the ground truth data very easily, while the annotation is automatically performed via thresholding, rather than manually. Second, our method is label-free and does not rely on fluorescence signals as input. On the contrary, our method is built upon the capability of neural networks to extract label-free cell cycle markers from the quantitative phase map. Thus, the method can be applied to live cell samples over long periods of time without concerns of photobleaching or degraded cell viability due to chemical or phototoxicity. Third, our approach can be applied to large sample sizes consisting of entire fields of views and hundreds of cells. Since we formulated the task as semantic segmentation and trained our model on a dataset containing images with various cell counts, our method worked with FOVs containing up to hundreds of cells. Also, since the U-Net [149] style neural network is fully convolutional, our trained model can be applied to images with arbitrary size. Consequentially, the method can directly extend to other cell datasets or experiments with different cell confluency, as long as the magnification and numerical aperture stay the same.

During the development of our method, we followed standard protocols in the community [94, 145, 223-225], such as preparing a diverse enough training dataset, properly splitting the training, validation and test dataset, and closely monitoring the model loss convergence to ensure that our model can generalize [224, 226, 227]. We believe PICS-based instruments are well-suited for extending our generalizable method to different cell lines and imaging conditions as the effort to perform extra training is minimal [82]. Our typical training only takes approximately 20 hours, which can be further reduced by utilizing distributed training on advanced GPUs. Thus, we

55

envision that our proposed workflow is a valuable alternative to the existing methods for cell cycle

stage classification and eliminates the need for cell synchronization.

6. Conclusion

Recent advancements in QPI and deep learning have opened up an exciting frontier. This thesis presented the principle of PICS, a family of methods that combine deep learning and QPI, and its application in cell biology study. The label-free nature of QPI and deep learning makes it possible to study biological phenomenon previously limited by photobleaching or phototoxicity associated with fluorescence microscopy. We believe that PICS can be easily tailored to various sorts of biological problems.

We note that, however, the following measures should be taken when developing PICS-style methods or operating deep learning enhanced QPI systems to ensure quality of the resulting methods. First, deep learning methods also have limitations. They cannot extract nonexistent structures or features. For example, it would be problematic to apply deep learning to approximate ill-posed problems which lack uniqueness of solutions [59]. In those scenarios, the deep learning model will likely learn characteristics associated with the dataset used for development and hallucinate when presented with unseen new data. Second, all the deep learning methods should be carefully evaluated on a test dataset of sufficient size to ensure generalizability. For clinical applications, it is recommended to test the trained networks on a well-curated external dataset of appropriate size [228]. Such practices might be hard to achieve at present, for basic science applications, due to lack of standard measurements and benchmark datasets [59, 89]. Third, the development datasets should be carefully acquired as the trained models' performance is ultimately limited by the training data [229]. The issues within the training dataset could have long-term negative impacts to the application of trained models downstream. Data issues might be easier to locate and correct in domains where human experts can provide the ultimate ground truth (e.g., pathology). In biological related problems, where

fluorescence signals are usually used to generate the ground truth data, the sample preparation

procedure and experimental design have to be evaluated carefully as they might impact the

acquired data. It is also recently speculated that deep learning systems might benefit from

consuming raw data, e.g., data that might seem uninterpretable to human eyes, directly and more

investigations are going into the fusion of deep learning based image formation and image

interpretation [89]. Last but not least, the deep learning training procedure (including

hyperparameters, model architectures, and data splits) should be carefully noted for replicability

and more meaningful comparison among different trained models.

What we presented in this thesis aims to provide examples of not only the enhancement

deep learning can bring to both QPI data and QPI systems, but also the value that this synergy

between QPI and deep learning can bring to the broader field of imaging and biomedical

research. We envision that deep learning algorithms will continue to be relevant for enhancing

QPI methods as well as interpreting QPI data. Since most algorithms and models are already

open-sourced and companies like MATLAB are actively building easy-to-use interface for

applying such algorithms on any dataset, we believe the cost to try out deep learning methods

will continue to decrease. Thus, the research at the interface between QPI and deep learning will

continue to be highly multidisciplinary, application-driven, and data-dependent.

References

[1]   R. Hooke, *Micrographia: Or Some Physiological Descriptions of Minute Bodies Made by Magnifying Glasses, with Observations and Inquiries Thereupon*. Courier Corporation, 2003.

[2]   C. K. Rosenthal, "The Beginning," *Nature Cell Biology,* vol. 11, no. 1, pp. S6-S6, 2009.

[3]   D. J. Stephens and V. J. Allan, "Light Microscopy Techniques for Live Cell Imaging," *Science,* vol. 300, no. 5616, pp. 82-86, Apr 4 2003.

[4]   A. Heinrichs, "Stains and Fluorescent Dyes," *Nature Cell Biology,* vol. 11, no. 1, pp. S7-S7, 2009.

[5]   J. W. Lichtman and J. A. Conchello, "Fluorescence Microscopy," *Nature Methods,* vol. 2, no. 12, pp. 910-919, Dec 2005.

[6]   Y. Park, C. Depeursinge, and G. Popescu, "Quantitative Phase Imaging in Biomedicine," (in English), *Nature Photonics,* vol. 12, no. 10, pp. 578-589, Oct 2018.

[7]   N. Rusk, "The Fluorescence Microscope," *Nature Cell Biology,* vol. 11, no. 1, pp. S8-S9, 2009.

[8]   A. Diaspro, G. Chirico, C. Usai, P. Ramoino, and J. Dobrucki, "Photobleaching," in *Handbook of Biological Confocal Microscopy*: Springer, 2006, pp. 690-702.

[9]   J. Icha, M. Weber, J. C. Waters, and C. Norden, "Phototoxicity in Live Fluorescence Microscopy, and How to Avoid It," (in English), *Bioessays,* vol. 39, no. 8, p. 1700003, Aug 2017.

[10]   P. P. Laissue, R. A. Alghamdi, P. Tomancak, E. G. Reynaud, and H. Shroff, "Assessing Phototoxicity in Live Fluorescence Imaging," *Nature Methods,* vol. 14, no. 7, pp. 657-661, Jun 29 2017.

[11]   E. Abbe, "Beiträge Zur Theorie Des Mikroskops Und Der Mikroskopischen Wahrnehmung," *Archiv für mikroskopische Anatomie,* vol. 9, no. 1, pp. 413-468, 1873.

[12]   N. Blow, "Finding Phase," *Nature Cell Biology,* vol. 11, no. 1, pp. S9-S9, 2009.

[13]   F. Zernike, "Phase Contrast, a New Method for the Microscopic Observation of Transparent Objects Part Ii," (in English), *Physica,* vol. 9, no. 10, pp. 974-986, 1942.

[14]   F. Zernike, "How I Discovered Phase Contrast," (in English), *Science,* vol. 121, no. 3141, pp. 345-349, 1955.

[15]   R. Barer, "Interference Microscopy and Mass Determination," *Nature,* vol. 169, no. 4296, pp. 366-367, Mar 1 1952.

[16]   H. G. Davies and M. H. Wilkins, "Interference Microscopy and Mass Determination," *Nature,* vol. 169, no. 4300, p. 541, Mar 29 1952.

[17]   D. Gabor, "A New Microscopic Principle," *Nature,* vol. 161, no. 4098, p. 777, May 15 1948.

[18]   M. K. Kim, "Principles and Techniques of Digital Holographic Microscopy," *SPIE reviews,* vol. 1, no. 1, p. 018005, 2010.

[19]   U. Schnars, C. Falldorf, J. Watson, and W. Jüptner, "Digital Holography," in *Digital Holography and Wavefront Sensing*: Springer, 2015, pp. 39-68.

[20]   J. W. Goodman and R. W. Lawrence, "Digital Image Formation from Electronically Detected Holograms," (in English), *Applied Physics Letters,* vol. 11, no. 3, pp. 77-+, 1967.

[21]   G. Popescu, *Quantitative Phase Imaging of Cells and Tissues*. McGraw Hill Professional, 2011.

[22]   C. Hu and G. Popescu, "Quantitative Phase Imaging (Qpi) in Neuroscience," *IEEE Journal of Selected Topics in Quantum Electronics,* vol. 25, no. 1, pp. 1-9, 2018.

[23]   Y. Park *et al.*, "Refractive Index Maps and Membrane Dynamics of Human Red Blood Cells Parasitized by Plasmodium Falciparum," *Proceedings of the National Academy of Sciences of the United States of America,* vol. 105, no. 37, pp. 13730-13735, Sep 16 2008.

[24]   Y. Park *et al.*, "Static and Dynamic Light Scattering of Healthy and Malaria-Parasite Invaded Red Blood Cells," *Journal of Biomedical Optics,* vol. 15, no. 2, p. 020506, Mar-Apr 2010.

[25]   Y. Park, C. A. Best-Popescu, R. R. Dasari, and G. Popescu, "Light Scattering of Human Red Blood Cells During Metabolic Remodeling of the Membrane," *Journal of Biomedical Optics,* vol. 16, no. 1, p. 011013, Jan-Feb 2011.

[26]   Y. Jang, J. Jang, and Y. Park, "Dynamic Spectroscopic Phase Microscopy for Quantifying Hemoglobin Concentration and Dynamic Membrane Fluctuation in Red Blood Cells," *Optics Express,* vol. 20, no. 9, pp. 9673-9681, Apr 23 2012.

[27]   K. Kim, H. Yoon, M. Diez-Silva, M. Dao, R. R. Dasari, and Y. Park, "High-Resolution Three-Dimensional Imaging of Red Blood Cells Parasitized by Plasmodium Falciparum and in Situ Hemozoin Crystals Using Optical Diffraction Tomography," *Journal of Biomedical Optics,* vol. 19, no. 1, p. 011005, 2013.

[28]   G. Popescu *et al.*, "Optical Imaging of Cell Mass and Growth Dynamics," *American Journal of Physiology: Cell Physiology,* vol. 295, no. 2, pp. C538-544, Aug 2008.

[29]   B. Rappaz *et al.*, "Noninvasive Characterization of the Fission Yeast Cell Cycle by Monitoring Dry Mass with Digital Holographic Microscopy," *Journal of Biomedical Optics,* vol. 14, no. 3, p. 034049, May-Jun 2009.

[30]   M. Mir *et al.*, "Optical Measurement of Cycle-Dependent Cell Growth," *Proceedings of the National Academy of Sciences of the United States of America,* vol. 108, no. 32, pp. 13124-13129, Aug 9 2011.

[31]   J. Reed *et al.*, "Rapid, Massively Parallel Single-Cell Drug Response Measurements Via Live Cell Interferometry," *Biophysical Journal,* vol. 101, no. 5, pp. 1025-1031, Sep 7 2011.

[32]   P. Girshovitz and N. T. Shaked, "Generalized Cell Morphological Parameters Based on Interferometric Phase Microscopy and Their Application to Cell Life Cycle Characterization," (in English), *Biomedical Optics Express,* vol. 3, no. 8, pp. 1757-1773, Aug 1 2012.

[33]   M. E. Kandel, W. Lu, J. Liang, O. Aydin, T. A. Saif, and G. Popescu, "Cell-to-Cell Influence on Growth in Large Populations," *Biomedical Optics Express,* vol. 10, no. 9, pp. 4664-4675, Sep 1 2019.

[34]   Y. Li, M. J. Fanous, K. A. Kilian, and G. Popescu, "Quantitative Phase Imaging Reveals Matrix Stiffness-Dependent Growth and Migration of Cancer Cells," *Scientific Reports,* vol. 9, no. 1, p. 248, Jan 22 2019.

[35]   G. Popescu *et al.*, "Optical Measurement of Cell Membrane Tension," *Physical Review Letters,* vol. 97, no. 21, p. 218101, Nov 24 2006.

[36]   S. Oh *et al.*, "Label-Free Imaging of Membrane Potential Using Membrane Electromotility," (in English), *Biophysical Journal,* vol. 103, no. 1, pp. 11-18, Jul 3 2012.

[37]   A. A. Evans, B. Bhaduri, G. Popescu, and A. J. Levine, "Geometric Localization of Thermal Fluctuations in Red Blood Cells," *Proceedings of the National Academy of Sciences of the United States of America,* vol. 114, no. 11, pp. 2865-2870, Mar 14 2017.

[38]   R. Wang, Z. Wang, L. Millet, M. U. Gillette, A. J. Levine, and G. Popescu, "Dispersion-Relation Phase Spectroscopy of Intracellular Transport," *Optics Express,* vol. 19, no. 21, pp. 20571-20579, Oct 10 2011.

[39]   M. Mir *et al.*, "Label-Free Characterization of Emerging Human Neuronal Networks," *Scientific Reports,* vol. 4, no. 1, p. 4434, Mar 24 2014.

[40]   M. J. Fanous, Y. Li, M. E. Kandel, A. A. Abdeen, K. A. Kilian, and G. Popescu, "Effects of Substrate Patterning on Cellular Spheroid Growth and Dynamics Measured by Gradient Light Interference Microscopy (Glim)," *Journal of Biophotonics,* vol. 12, no. 12, p. e201900178, Dec 2019.

[41]   J. Andrecka, J. O. Arroyo, K. Lewis, R. A. Cross, and P. Kukura, "Label-Free Imaging of Microtubules with Sub-Nm Precision Using Interferometric Scattering Microscopy," *Biophysical Journal,* vol. 110, no. 1, pp. 214-217, 2016.

[42]   M. E. Kandel, K. W. Teng, P. R. Selvin, and G. Popescu, "Label-Free Imaging of Single Microtubule Dynamics Using Spatial Light Interference Microscopy," (in English), *ACS Nano,* vol. 11, no. 1, pp. 647-655, Jan 24 2017.

[43]   P. Jourdain *et al.*, "Determination of Transmembrane Water Fluxes in Neurons Elicited by Glutamate Ionotropic Receptors and by the Cotransporters Kcc2 and Nkcc1: A Digital Holographic Microscopy Study," *Journal of Neuroscience,* vol. 31, no. 33, pp. 11846-11854, Aug 17 2011.

[44]   P. Marquet, C. Depeursinge, and P. J. Magistretti, "Review of Quantitative Phase-Digital Holographic Microscopy: Promising Novel Imaging Technique to Resolve Neuronal Network Activity and Identify Cellular Biomarkers of Psychiatric Disorders," *Neurophotonics,* vol. 1, no. 2, p. 020901, Oct 2014.

[45]   Y. J. Lee *et al.*, "Quantitative Assessment of Neural Outgrowth Using Spatial Light Interference Microscopy," (in English), *Journal of Biomedical Optics,* vol. 22, no. 6, p. 66015, Jun 1 2017.

[46]   T. W. Su, L. Xue, and A. Ozcan, "High-Throughput Lensfree 3d Tracking of Human Sperms Reveals Rare Statistics of Helical Trajectories," *Proceedings of the National Academy of Sciences of the United States of America,* vol. 109, no. 40, pp. 16018-16022, Oct 2 2012.

[47]   F. Merola *et al.*, "Digital Holography as a Method for 3d Imaging and Estimating the Biovolume of Motile Cells," (in English), *Lab Chip,* vol. 13, no. 23, pp. 4512-4516, Dec 7 2013.

[48]   G. Di Caprio *et al.*, "Holographic Imaging of Unlabelled Sperm Cells for Semen Analysis: A Review," *Journal of Biophotonics,* vol. 8, no. 10, pp. 779-789, Oct 2015.

[49]   H. Ding, F. Nguyen, S. A. Boppart, and G. Popescu, "Optical Properties of Tissues Quantified by Fourier-Transform Light Scattering," *Optics Letters,* vol. 34, no. 9, pp. 1372-1374, May 1 2009.

[50]   P. Wang *et al.*, "Nanoscale Nuclear Architecture for Cancer Diagnosis Beyond Pathology Via Spatial-Domain Low-Coherence Quantitative Phase Microscopy," *Journal of Biomedical Optics,* vol. 15, no. 6, p. 066028, Nov-Dec 2010.

[51]   M. Fanous, A. Keikhosravi, A. Kajdacsy-Balla, K. W. Eliceiri, and G. Popescu, "Quantitative Phase Imaging of Stromal Prognostic Markers in Pancreatic Ductal Adenocarcinoma," *Biomedical Optics Express,* vol. 11, no. 3, pp. 1354-1364, Mar 1 2020.

[52]   T. H. Nguyen, M. E. Kandel, M. Rubessa, M. B. Wheeler, and G. Popescu, "Gradient Light Interference Microscopy for 3d Imaging of Unlabeled Specimens," *Nature Communications,* vol. 8, no. 1, p. 210, Aug 8 2017.

[53]   M. E. Kandel *et al.*, "Epi-Illumination Gradient Light Interference Microscopy for Imaging Opaque Structures," *Nature Communications,* vol. 10, no. 1, p. 4691, Oct 16 2019.

[54]   E. Wolf, "Three-Dimensional Structure Determination of Semi-Transparent Objects from Holographic Data," *Optics Communications,* vol. 1, no. 4, pp. 153-156, 1969.

[55]   F. Charriere *et al.*, "Cell Refractive Index Tomography by Digital Holographic Microscopy," (in English), *Optics Letters,* vol. 31, no. 2, pp. 178-180, Jan 15 2006.

[56]   T. Kim *et al.*, "White-Light Diffraction Tomography of Unlabelled Live Cells," (in English), *Nature Photonics,* vol. 8, no. 3, pp. 256-263, Mar 2014.

[57]   C. F. Hu *et al.*, "Harmonic Optical Tomography of Nonlinear Structures," (in English), *Nature Photonics,* vol. 14, no. 9, pp. 564-+, Sep 2020.

[58]   K. Kim, K. S. Kim, H. Park, J. C. Ye, and Y. Park, "Real-Time Visualization of 3-D Dynamic Microscopic Objects Using Optical Diffraction Tomography," (in English), *Optics Express,* vol. 21, no. 26, pp. 32269-32278, Dec 30 2013.

[59]   Y. Jo *et al.*, "Quantitative Phase Imaging and Artificial Intelligence: A Review," *IEEE Journal of Selected Topics in Quantum Electronics,* vol. 25, no. 1, pp. 1-14, 2018.

[60]   Y. LeCun, Y. Bengio, and G. Hinton, "Deep Learning," *Nature,* vol. 521, no. 7553, pp. 436-444, May 28 2015.

[61]   C. M. Bishop, "Pattern Recognition," *Machine learning,* vol. 128, no. 9, 2006.
[62]   D. E. Rumelhart, G. E. Hinton, and R. J. Williams, "Learning Representations by Back-Propagating Errors," (in English), *Nature,* vol. 323, no. 6088, pp. 533-536, Oct 9 1986.
[63]   P. Werbos, "Beyond Regression:" New Tools for Prediction and Analysis in the Behavioral Sciences," *Ph. D. dissertation, Harvard University,* 1974.
[64]   G. E. Hinton and R. R. Salakhutdinov, "Reducing the Dimensionality of Data with Neural Networks," *Science,* vol. 313, no. 5786, pp. 504-507, Jul 28 2006.
[65]   P. Sermanet, K. Kavukcuoglu, S. Chintala, and Y. LeCun, "Pedestrian Detection with Unsupervised Multi-Stage Feature Learning," in *Proceedings of the IEEE conference on computer vision and pattern recognition*, 2013, pp. 3626-3633.
[66]   J. Sanders and E. Kandrot, *Cuda by Example: An Introduction to General-Purpose Gpu Programming*. Addison-Wesley Professional, 2010.
[67]   R. Raina, A. Madhavan, and A. Y. Ng, "Large-Scale Deep Unsupervised Learning Using Graphics Processors," in *Proceedings of the 26th annual international conference on machine learning*, 2009, pp. 873-880.
[68]   G. E. Dahl, D. Yu, L. Deng, and A. Acero, "Context-Dependent Pre-Trained Deep Neural Networks for Large-Vocabulary Speech Recognition," *IEEE Transactions on Audio, Speech, and Language Processing,* vol. 20, no. 1, pp. 30-42, 2011.
[69]   Y. LeCun *et al.*, "Handwritten Digit Recognition with a Back-Propagation Network," *Advances in Neural Information Processing Systems,* vol. 2, 1989.
[70]   D. H. Hubel and T. N. Wiesel, "Receptive Fields, Binocular Interaction and Functional Architecture in the Cat's Visual Cortex," *Journal of Physiology,* vol. 160, no. 1, pp. 106-154, Jan 1962.
[71]   D. J. Felleman and D. C. Van Essen, "Distributed Hierarchical Processing in the Primate Cerebral Cortex," *Cerebral Cortex,* vol. 1, no. 1, pp. 1-47, Jan-Feb 1991.
[72]   W. Rawat and Z. Wang, "Deep Convolutional Neural Networks for Image Classification: A Comprehensive Review," *Neural Computation,* vol. 29, no. 9, pp. 2352-2449, Sep 2017.
[73]   O. Russakovsky *et al.*, "Imagenet Large Scale Visual Recognition Challenge," (in English), *International Journal of Computer Vision,* vol. 115, no. 3, pp. 211-252, Dec 2015.
[74]   A. Krizhevsky, I. Sutskever, and G. E. Hinton, "Imagenet Classification with Deep Convolutional Neural Networks," *Advances in Neural Information Processing Systems,* vol. 25, pp. 1097-1105, 2012.
[75]   R. Girshick, J. Donahue, T. Darrell, and J. Malik, "Rich Feature Hierarchies for Accurate Object Detection and Semantic Segmentation," in *Proceedings of the IEEE conference on computer vision and pattern recognition*, 2014, pp. 580-587.
[76]   P. Sermanet, D. Eigen, X. Zhang, M. Mathieu, R. Fergus, and Y. LeCun, "Overfeat: Integrated Recognition, Localization and Detection Using Convolutional Networks," *arXiv preprint arXiv:1312.6229,* 2013.
[77]   K. Simonyan and A. Zisserman, "Very Deep Convolutional Networks for Large-Scale Image Recognition," *arXiv preprint arXiv:1409.1556,* 2014.
[78]   Y. Jo *et al.*, "Holographic Deep Learning for Rapid Optical Screening of Anthrax Spores," *Science Advances,* vol. 3, no. 8, p. e1700606, Aug 2017.
[79]   Y. Rivenson, T. Liu, Z. Wei, Y. Zhang, K. de Haan, and A. Ozcan, "Phasestain: The Digital Staining of Label-Free Quantitative Phase Microscopy Images Using Deep Learning," (in English), *Light: Science & Applications,* vol. 8, no. 1, p. 23, Feb 6 2019.
[80]   E. M. Christiansen *et al.*, "In Silico Labeling: Predicting Fluorescent Labels in Unlabeled Images," *Cell,* vol. 173, no. 3, pp. 792-803 e719, Apr 19 2018.

[81]   C. Ounkomol, S. Seshamani, M. M. Maleckar, F. Collman, and G. R. Johnson, "Label-Free Prediction of Three-Dimensional Fluorescence Images from Transmitted-Light Microscopy," *Nature Methods,* vol. 15, no. 11, pp. 917-920, Nov 2018.

[82]   M. E. Kandel *et al.*, "Phase Imaging with Computational Specificity (Pics) for Measuring Dry Mass Changes in Sub-Cellular Compartments," *Nature Communications,* vol. 11, no. 1, p. 6256, Dec 7 2020.

[83]   M. E. Kandel *et al.*, "Reproductive Outcomes Predicted by Phase Imaging with Computational Specificity of Spermatozoon Ultrastructure," *Proceedings of the National Academy of Sciences of the United States of America,* vol. 117, no. 31, pp. 18302-18309, Aug 4 2020.

[84]   C. Hu *et al.*, "Live-Dead Assay on Unlabeled Cells Using Phase Imaging with Computational Specificity," *bioRxiv,* p. 2020.2010. 2028.359554, 2021.

[85]   M. E. Kandel, E. Kim, Y. J. Lee, G. Tracy, H. J. Chung, and G. Popescu, "Multiscale Assay of Unlabeled Neurite Dynamics Using Phase Imaging with Computational Specificity," (in English), *ACS Sensors,* vol. 6, no. 5, pp. 1864-1874, May 28 2021.

[86]   M. D. Hannel, A. Abdulali, M. O'Brien, and D. G. Grier, "Machine-Learning Techniques for Fast and Accurate Feature Localization in Holograms of Colloidal Particles," *Optics Express,* vol. 26, no. 12, pp. 15221-15231, Jun 11 2018.

[87]   F. Yi, I. Moon, and B. Javidi, "Automated Red Blood Cells Extraction from Holographic Images Using Fully Convolutional Neural Networks," (in English), *Biomedical Optics Express,* vol. 8, no. 10, pp. 4466-4479, Oct 1 2017.

[88]   M. Bertero and P. Boccacci, *Introduction to Inverse Problems in Imaging*. CRC press, 2020.

[89]   G. Barbastathis, A. Ozcan, and G. Situ, "On the Use of Deep Learning for Computational Imaging," (in English), *Optica,* vol. 6, no. 8, pp. 921-943, Aug 20 2019.

[90]   Y. Rivenson, Z. Gorocs, H. Gunaydin, Y. B. Zhang, H. D. Wang, and A. Ozcan, "Deep Learning Microscopy," (in English), *Optica,* vol. 4, no. 11, pp. 1437-1443, Nov 20 2017.

[91]   Y. C. Wu *et al.*, "Extended Depth-of-Field in Holographic Imaging Using Deep-Learning-Based Autofocusing and Phase Recovery," (in English), *Optica,* vol. 5, no. 6, pp. 704-710, Jun 20 2018.

[92]   T. Nguyen, V. Bui, and G. Nehmetallah, "Computational Optical Tomography Using 3-D Deep Convolutional Neural Networks," (in English), *Optical Engineering,* vol. 57, no. 4, p. 043111, Apr 2018.

[93]   Z. Ren, Z. Xu, and E. Y. Lam, "Learning-Based Nonparametric Autofocusing for Digital Holography," *Optica,* vol. 5, no. 4, pp. 337-344, 2018.

[94]   H. Pinkard, Z. Phillips, A. Babakhani, D. A. Fletcher, and L. Waller, "Deep Learning for Single-Shot Autofocus Microscopy," (in English), *Optica,* vol. 6, no. 6, pp. 794-797, Jun 20 2019.

[95]   T. Nguyen, V. Bui, V. Lam, C. B. Raub, L. C. Chang, and G. Nehmetallah, "Automatic Phase Aberration Compensation for Digital Holographic Microscopy Based on Deep Learning Background Detection," *Optics Express,* vol. 25, no. 13, pp. 15043-15057, Jun 26 2017.

[96]   L. Mockl, A. R. Roy, P. N. Petrov, and W. E. Moerner, "Accurate and Rapid Background Estimation in Single-Molecule Localization Microscopy Using the Deep Neural Network Bgnet," (in English), *Proceedings of the National Academy of Sciences of the United States of America,* vol. 117, no. 1, pp. 60-67, Jan 7 2020.

[97]   Y. H. Jiao, Y. C. R. He, M. E. Kandel, X. J. Liu, W. L. Lu, and G. Popescu, "Computational Interference Microscopy Enabled by Deep Learning," (in English), *APL Photonics,* vol. 6, no. 4, p. 046103, Apr 1 2021.

[98]   M. Mir, B. Bhaduri, R. Wang, R. Y. Zhu, and G. Popescu, "Quantitative Phase Imaging," (in English), *Progress in Optics, Vol 57,* vol. 57, no. 133-37, pp. 133-217, 2012.

[99]   G. Popescu, T. Ikeda, R. R. Dasari, and M. S. Feld, "Diffraction Phase Microscopy for Quantifying Cell Structure and Dynamics," *Optics Letters,* vol. 31, no. 6, pp. 775-777, Mar 15 2006.

[100]   B. Bhaduri, H. Pham, M. Mir, and G. Popescu, "Diffraction Phase Microscopy with White Light," *Optics Letters,* vol. 37, no. 6, pp. 1094-1096, Mar 15 2012.

[101]   B. Bhaduri *et al.*, "Diffraction Phase Microscopy: Principles and Applications in Materials and Life Sciences," (in English), *Advances in Optics and Photonics,* vol. 6, no. 1, pp. 57-119, Mar 2014.

[102]   T. Ikeda, G. Popescu, R. R. Dasari, and M. S. Feld, "Hilbert Phase Microscopy for Investigating Fast Dynamics in Transparent Systems," *Optics Letters,* vol. 30, no. 10, pp. 1165-1167, May 15 2005.

[103]   H. Majeed *et al.*, "Magnified Image Spatial Spectrum (Miss) Microscopy for Nanometer and Millisecond Scale Label-Free Imaging," *Optics Express,* vol. 26, no. 5, pp. 5423-5440, Mar 5 2018.

[104]   P. Bon, G. Maucort, B. Wattellier, and S. Monneret, "Quadriwave Lateral Shearing Interferometry for Quantitative Phase Microscopy of Living Cells," *Optics Express,* vol. 17, no. 15, pp. 13080-13094, Jul 20 2009.

[105]   P. Kolman and R. Chmelik, "Coherence-Controlled Holographic Microscope," *Optics Express,* vol. 18, no. 21, pp. 21990-22003, Oct 11 2010.

[106]   L. W. Zhu *et al.*, "Femtosecond Off-Axis Digital Holography for Monitoring Dynamic Surface Deformation," (in English), *Applied Optics,* vol. 49, no. 13, pp. 2510-2518, May 1 2010.

[107]   G. Popescu *et al.*, "Fourier Phase Microscopy for Investigation of Biological Structures and Dynamics," *Optics Letters,* vol. 29, no. 21, pp. 2503-2505, Nov 1 2004.

[108]   Z. Wang *et al.*, "Spatial Light Interference Microscopy (Slim)," *Optics Express,* vol. 19, no. 2, pp. 1016-1026, Jan 17 2011.

[109]   X. Chen, M. E. Kandel, and G. Popescu, "Spatial Light Interference Microscopy: Principle and Applications to Biomedicine," *Advances in Optics and Photonics,* vol. 13, no. 2, pp. 353-425, 2021.

[110]   K. Lee and Y. Park, "Quantitative Phase Imaging Unit," *Optics Letters,* vol. 39, no. 12, pp. 3630-3633, Jun 15 2014.

[111]   W. S. Rockward, A. L. Thomas, B. Zhao, and C. A. DiMarzio, "Quantitative Phase Measurements Using Optical Quadrature Microscopy," (in English), *Applied Optics,* vol. 47, no. 10, pp. 1684-1696, Apr 1 2008.

[112]   D. Zicha and G. A. Dunn, "An Image-Processing System for Cell Behavior Studies in Subconfluent Cultures," (in English), *Journal of Microscopy-Oxford,* vol. 179, no. 1, pp. 11-21, Jul 1995.

[113]   C. Hu *et al.*, "Optical Excitation and Detection of Neuronal Activity," *Journal of Biophotonics,* vol. 12, no. 3, p. e201800269, Mar 2019.

[114]   H. V. Pham, B. Bhaduri, K. Tangella, C. Best-Popescu, and G. Popescu, "Real Time Blood Testing Using Quantitative Phase Imaging," (in English), *PloS One,* vol. 8, no. 2, p. e55676, Feb 6 2013.

[115]   R. J. Zhou, C. Edwards, A. Arbabi, G. Popescu, and L. L. Goddard, "Detecting 20 Nm Wide Defects in Large Area Nanopatterns Using Optical Interferometric Microscopy," (in English), *Nano Letters,* vol. 13, no. 8, pp. 3716-3721, Aug 2013.

[116]   R. Zhou, C. Edwards, G. Popescu, and L. L. Goddard, "9nm Node Wafer Defect Inspection Using Visible Light," in *Metrology, Inspection, and Process Control for Microlithography XXVIII*, 2014, vol. 9050, p. 905017: International Society for Optics and Photonics.

[117]   R. Zhou, G. Popescu, and L. L. Goddard, "22 Nm Node Wafer Inspection Using Diffraction Phase Microscopy and Image Post-Processing," in *Metrology, Inspection, and Process Control for Microlithography XXVII*, 2013, vol. 8681, p. 86810G: International Society for Optics and Photonics.

[118]   C. Edwards, B. Bhaduri, B. G. Griffin, L. L. Goddard, and G. Popescu, "Epi-Illumination Diffraction Phase Microscopy with White Light," *Optics Letters,* vol. 39, no. 21, pp. 6162-6165, Nov 1 2014.

[119]   D. B. Kirk and W. H. Wen-Mei, *Programming Massively Parallel Processors: A Hands-on Approach*. Morgan kaufmann, 2016.

[120]   H. Pham, H. F. Ding, N. Sobh, M. Do, S. Patel, and G. Popescu, "Off-Axis Quantitative Phase Imaging Processing Using Cuda: Toward Real-Time Applications," (in English), *Biomedical Optics Express,* vol. 2, no. 7, pp. 1781-1793, Jul 1 2011.

[121]   B. Bhaduri and G. Popescu, "Derivative Method for Phase Retrieval in Off-Axis Quantitative Phase Imaging," *Optics Letters,* vol. 37, no. 11, pp. 1868-1870, Jun 1 2012.

[122]   K. Chu, Z. J. Smith, S. Wachsmann-Hogiu, and S. Lane, "Super-Resolved Spatial Light Interference Microscopy," *Journal of the Optical Society of America A: Optics, Image Science, and Vision,* vol. 29, no. 3, pp. 344-351, Mar 1 2012.

[123]   X. Fan, Z. Tang, J. J. Healy, K. O'Dwyer, and B. M. Hennelly, "Label-Free Rheinberg Staining of Cells Using Digital Holographic Microscopy and Spatial Light Interference Microscopy," in *Advanced Optical Imaging Technologies II*, 2019, vol. 11186, p. 111860D: International Society for Optics and Photonics.

[124]   H. Majeed, T. H. Nguyen, M. E. Kandel, A. Kajdacsy-Balla, and G. Popescu, "Label-Free Quantitative Evaluation of Breast Tissue Using Spatial Light Interference Microscopy (Slim)," (in English), *Scientific Reports,* vol. 8, no. 1, pp. 1-9, May 2 2018.

[125]   Z. Wang *et al.*, "Topography and Refractometry of Nanostructures Using Spatial Light Interference Microscopy," (in English), *Optics Letters,* vol. 35, no. 2, pp. 208-210, Jan 15 2010.

[126]   S. D. Babacan, Z. Wang, M. Do, and G. Popescu, "Cell Imaging Beyond the Diffraction Limit Using Sparse Deconvolution Spatial Light Interference Microscopy," (in English), *Biomedical Optics Express,* vol. 2, no. 7, pp. 1815-1827, Jul 1 2011.

[127]   H. Majeed *et al.*, "Quantitative Histopathology of Stained Tissues Using Color Spatial Light Interference Microscopy (Cslim)," (in English), *Scientific Reports,* vol. 9, no. 1, p. 14679, Oct 11 2019.

[128]   T. H. Nguyen, C. Edwards, L. L. Goddard, and G. Popescu, "Quantitative Phase Imaging with Partially Coherent Illumination," *Optics Letters,* vol. 39, no. 19, pp. 5511-5514, Oct 1 2014.

[129]   M. E. Kandel, M. Fanous, C. Best-Popescu, and G. Popescu, "Real-Time Halo Correction in Phase Contrast Imaging," *Biomedical Optics Express,* vol. 9, no. 2, pp. 623-635, Feb 1 2018.

[130]   T. H. Nguyen *et al.*, "Halo-Free Phase Contrast Microscopy," *Scientific Reports,* vol. 7, no. 1, p. 44034, Mar 24 2017.

[131]   A. Fan, A. Tofangchi, M. Kandel, G. Popescu, and T. Saif, "Coupled Circumferential and Axial Tension Driven by Actin and Myosin Influences in Vivo Axon Diameter," *Scientific Reports,* vol. 7, no. 1, p. 14188, Oct 27 2017.

[132]   S. Sridharan, M. Mir, and G. Popescu, "Simultaneous Optical Measurements of Cell Motility and Growth," *Biomedical Optics Express,* vol. 2, no. 10, pp. 2815-2820, Oct 1 2011.

[133]   Z. Wang, K. Tangella, A. Balla, and G. Popescu, "Tissue Refractive Index as Marker of Disease," (in English), *Journal of Biomedical Optics,* vol. 16, no. 11, p. 116017, Nov 2011.

[134]   H. Ding, Z. Wang, X. Liang, S. A. Boppart, K. Tangella, and G. Popescu, "Measuring the Scattering Parameters of Tissues from Quantitative Phase Imaging of Thin Slices," *Optics Letters,* vol. 36, no. 12, pp. 2281-2283, Jun 15 2011.

[135]   S. Sridharan, V. Macias, K. Tangella, A. Kajdacsy-Balla, and G. Popescu, "Prediction of Prostate Cancer Recurrence Using Quantitative Phase Imaging," (in English), *Scientific Reports,* vol. 5, no. 1, p. 9976, May 15 2015.

[136]   S. Sridharan *et al.*, "Prediction of Prostate Cancer Recurrence Using Quantitative Phase Imaging: Validation on a General Population," (in English), *Scientific Reports,* vol. 6, no. 1, pp. 1-9, Sep 23 2016.

[137]   B. Bhaduri, M. Kandel, C. Brugnara, K. Tangella, and G. Popescu, "Optical Assay of Erythrocyte Function in Banked Blood," *Scientific Reports,* vol. 4, no. 1, p. 6211, Sep 5 2014.

[138]   M. Rubessa, S. N. Lotti, M. E. Kandel, G. Popescu, and M. B. Wheeler, "Slim Microscopy Allows for Visualization of DNA-Containing Liposomes Designed for Sperm-Mediated Gene Transfer in Cattle," *Molecular Biology Reports,* vol. 46, no. 1, pp. 695-703, Feb 2019.

[139]   X. Chen, M. E. Kandel, C. Hu, Y. J. Lee, and G. Popescu, "Wolf Phase Tomography (Wpt) of Transparent Structures Using Partially Coherent Illumination," (in English), *Light: Science & Applications,* vol. 9, no. 1, p. 142, Aug 19 2020.

[140]   L. Mandel and E. Wolf, "Coherence Properties of Optical Fields," (in English), *Reviews of Modern Physics,* vol. 37, no. 2, pp. 231-+, 1965.

[141]   A. Lasslett, "Principles and Applications of Differential Interference Contrast Light Microscopy," *Microscopy and Analysis,* vol. 20, no. 5, pp. S9-S11, 2006.

[142]   M. Shribak, "Quantitative Orientation-Independent Dic Microscopy with High Speed Switching Shear Direction," in *Biomedical Optics*, 2010, p. BTuD79: Optical Society of America.

[143]   N. Goswami *et al.*, "Monitoring Reactivation of Latent Hiv by Label-Free Gradient Light Interference Microscopy," *bioRxiv,* 2020.

[144]   P. Isola, J.-Y. Zhu, T. Zhou, and A. A. Efros, "Image-to-Image Translation with Conditional Adversarial Networks," in *Proceedings of the IEEE conference on computer vision and pattern recognition*, 2017, pp. 1125-1134.

[145]   Y. Rivenson *et al.*, "Virtual Histological Staining of Unlabelled Tissue-Autofluorescence Images Via Deep Learning," *Nature Biomedical Engineering,* vol. 3, no. 6, pp. 466-477, Jun 2019.

[146]   Y. N. Nygate *et al.*, "Holographic Virtual Staining of Individual Biological Cells," *Proceedings of the National Academy of Sciences of the United States of America,* vol. 117, no. 17, pp. 9223-9231, Apr 28 2020.

[147]   J. C. Waters, "Accuracy and Precision in Quantitative Fluorescence Microscopy," ed: The Rockefeller University Press, 2009.

[148]   A. Sakaue-Sawano *et al.*, "Genetically Encoded Tools for Optical Dissection of the Mammalian Cell Cycle," *Molecular Cell,* vol. 68, no. 3, pp. 626-640 e625, Nov 2 2017.

[149]   O. Ronneberger, P. Fischer, and T. Brox, "U-Net: Convolutional Networks for Biomedical Image Segmentation," in *International Conference on Medical Image Computing and Computer-Assisted Intervention*, 2015, pp. 234-241: Springer.

[150]   T. Falk *et al.*, "U-Net: Deep Learning for Cell Counting, Detection, and Morphometry," *Nature Methods,* vol. 16, no. 1, pp. 67-70, 2019.

[151]   S. Ioffe and C. Szegedy, "Batch Normalization: Accelerating Deep Network Training by Reducing Internal Covariate Shift," in *International Conference on Machine Learning*, 2015, pp. 448-456: PMLR.

[152]   K. He, X. Zhang, S. Ren, and J. Sun, "Deep Residual Learning for Image Recognition," in *Proceedings of the IEEE conference on computer vision and pattern recognition*, 2016, pp. 770-778.

[153]   Z. C. Lipton, "The Mythos of Model Interpretability: In Machine Learning, the Concept of Interpretability Is Both Important and Slippery," *Queue,* vol. 16, no. 3, pp. 31-57, 2018.

[154]   Q. S. Zhang and S. C. Zhu, "Visual Interpretability for Deep Learning: A Survey," (in English), *Frontiers of Information Technology & Electronic Engineering,* vol. 19, no. 1, pp. 27-39, Jan 2018.

[155]   R. R. Selvaraju, M. Cogswell, A. Das, R. Vedantam, D. Parikh, and D. Batra, "Grad-Cam: Visual Explanations from Deep Networks Via Gradient-Based Localization," in *Proceedings of the IEEE international conference on computer vision*, 2017, pp. 618-626.

[156]   K. Vinogradova, A. Dibrov, and G. Myers, "Towards Interpretable Semantic Segmentation Via Gradient-Weighted Class Activation Mapping," *arXiv preprint arXiv:2002.11434,* 2020.

[157]   M. Du, N. Liu, and X. Hu, "Techniques for Interpretable Machine Learning," *Communications of the ACM,* vol. 63, no. 1, pp. 68-77, 2019.

[158]   NVIDIA, "Initializing the Engine," in *Best Practices for Tensorrt Performance*, p. 9.

[159]   H. Vanholder, "Efficient Inference with Tensorrt," ed: ed, 2016.

[160]   J. Bai, F. Lu, and K. Zhang, "Onnx: Open Neural Network Exchange," *GitHub repository,* 2019.

[161]   H. Group, "Hierarchical Data Format Version 5," 1997.

[162]   M. Abadi *et al.*, "Tensorflow: Large-Scale Machine Learning on Heterogeneous Distributed Systems," *arXiv preprint arXiv:1603.04467,* 2016.

[163]   B. A. Edgar, C. P. Kiehle, and G. Schubiger, "Cell Cycle Control by the Nucleo-Cytoplasmic Ratio in Early Drosophila Development," *Cell,* vol. 44, no. 2, pp. 365-372, Jan 31 1986.

[164]   D. J. Brennan *et al.*, "Altered Cytoplasmic-to-Nuclear Ratio of Survivin Is a Prognostic Indicator in Breast Cancer," (in English), *Clinical Cancer Research,* vol. 14, no. 9, pp. 2681-2689, May 1 2008.

[165]   W. W. Sung *et al.*, "High Nuclear/Cytoplasmic Ratio of Cdk1 Expression Predicts Poor Prognosis in Colorectal Cancer Patients," *BMC Cancer,* vol. 14, no. 1, p. 951, Dec 15 2014.

[166]   T. S and C. M. (2016). *How to Do a Proper Cell Culture Quick Check : Workflow for Subculture of Adherent Cells* Available: https://www.leica-microsystems.com/science-lab/how-to-do-a-proper-cell-culture-quick-check/

[167]   M. V. Meng, K. L. Greene, and P. J. Turek, "Surgery or Assisted Reproduction? A Decision Analysis of Treatment Costs in Male Infertility," (in eng), *Journal of Urology,* vol. 174, no. 5, pp. 1926-1931; discussion 1931, Nov 2005.

[168]   M. Nadalini, N. Tarozzi, V. Distratis, G. Scaravelli, and A. Borini, "Impact of Intracytoplasmic Morphologically Selected Sperm Injection on Assisted Reproduction Outcome: A Review," *Reprod Biomed Online,* vol. 19 Suppl 3, pp. 45-55, 2009.

[169]   A. Berkovitz *et al.*, "How to Improve Ivf–Icsi Outcome by Sperm Selection," *Reproductive biomedicine online,* vol. 12, no. 5, pp. 634-638, 2006.

[170]   P. Vanderzwalmen *et al.*, "Intracytoplasmic Morphologically Selected Sperm Injection," in *In Vitro Fertilization*: Springer, 2019, pp. 415-428.

[171]   S. Kondracki, A. Wysokinska, M. Kania, and K. Gorski, "Application of Two Staining Methods for Sperm Morphometric Evaluation in Domestic Pigs," (in eng), *Journal of Veterinary Research,* vol. 61, no. 3, pp. 345-349, Sep 2017.

[172]   D. Banaszewska, K. Andraszek, M. Czubaszek, and B. Biesiada-Drzazga, "The Effect of Selected Staining Techniques on Bull Sperm Morphometry," (in eng), *Animal Reproduction Science,* vol. 159, pp. 17-24, Aug 2015.

[173]   L. Maree, S. S. du Plessis, R. Menkveld, and G. van der Horst, "Morphometric Dimensions of the Human Sperm Head Depend on the Staining Method Used," (in eng), *Human Reproduction,* vol. 25, no. 6, pp. 1369-1382, Jun 2010.

[174]   G. Nomarski, "Microinterféromètre Différentiel À Ondes Polarisées," *Journal de Physique et le Radium,* vol. 16, no. 3, pp. 9S-13S, 1955.

[175]   R. Hoffman and L. Gross, "Modulation Contrast Microscope," *Applied Optics,* vol. 14, no. 5, pp. 1169-1176, 1975.

[176]   L. Liu, M. E. Kandel, M. Rubessa, S. Schreiber, M. B. Wheeler, and G. Popescu, "Topography and Refractometry of Sperm Cells Using Spatial Light Interference Microscopy," *Journal of Biomedical Optics,* vol. 23, no. 2, p. 025003, 2018.

[177]   L. Miccio *et al.*, "Detection and Visualization Improvement of Spermatozoa Cells by Digital Holography," in *European Conference on Biomedical Optics*, 2011, p. 80890C: Optical Society of America.

[178]   M. Haifler, P. Girshovitz, G. Band, G. Dardikman, I. Madjar, and N. T. Shaked, "Interferometric Phase Microscopy for Label-Free Morphological Evaluation of Sperm Cells," *Fertility and Sterility,* vol. 104, no. 1, pp. 43-47. e42, 2015.

[179] P. Memmolo *et al.*, "Identification of Bovine Sperm Head for Morphometry Analysis in Quantitative Phase-Contrast Holographic Microscopy," *Optics Express,* vol. 19, no. 23, pp. 23215-23226, Nov 7 2011.

[180] G. Di Caprio *et al.*, "4d Tracking of Clinical Seminal Samples for Quantitative Characterization of Motility Parameters," *Biomedical Optics Express,* vol. 5, no. 3, pp. 690-700, Mar 1 2014.

[181] Y. Sasaki, "The Truth of the F-Measure. 2007," ed, 2007.

[182] R. M. Haralick and L. G. Shapiro, *Computer and Robot Vision*. Addison-wesley Reading, 1992.

[183] B. Balaban, K. Lundin, J. Morrell, H. Tjellström, B. Urman, and P. Holmes, "An Alternative to Pvp for Slowing Sperm Prior to Icsi," *Human Reproduction,* vol. 18, no. 9, pp. 1887-1889, 2003.

[184] N. Srivastava, G. Hinton, A. Krizhevsky, I. Sutskever, and R. Salakhutdinov, "Dropout: A Simple Way to Prevent Neural Networks from Overfitting," (in English), *Journal of Machine Learning Research,* vol. 15, no. 1, pp. 1929-1958, Jun 2014.

[185] D. P. Kingma and J. Ba, "Adam: A Method for Stochastic Optimization," *arXiv preprint arXiv:1412.6980,* 2014.

[186] K. A. Schafer, "The Cell Cycle: A Review," *Veterinary Pathology,* vol. 35, no. 6, pp. 461-478, Nov 1998.

[187] M. B. Kastan and J. Bartek, "Cell-Cycle Checkpoints and Cancer," *Nature,* vol. 432, no. 7015, pp. 316-323, Nov 18 2004.

[188] M. Malumbres and M. Barbacid, "Cell Cycle, Cdks and Cancer: A Changing Paradigm," *Nature Reviews: Cancer,* vol. 9, no. 3, pp. 153-166, Mar 2009.

[189] S. J. Elledge, "Cell Cycle Checkpoints: Preventing an Identity Crisis," *Science,* vol. 274, no. 5293, pp. 1664-1672, Dec 6 1996.

[190] H. Lodish *et al.*, *Molecular Cell Biology*. Macmillan, 2008.

[191] G. Maga and U. Hubscher, "Proliferating Cell Nuclear Antigen (Pcna): A Dancer with Many Partners," *Journal of Cell Science,* vol. 116, no. Pt 15, pp. 3051-3060, Aug 1 2003.

[192] Z. Kelman, "Pcna: Structure, Functions and Interactions," *Oncogene,* vol. 14, no. 6, pp. 629-640, Feb 13 1997.

[193] M. Wang, X. Zhou, F. Li, J. Huckins, R. W. King, and S. T. Wong, "Novel Cell Segmentation and Online Svm for Cell Cycle Phase Identification in Automated Microscopy," *Bioinformatics,* vol. 24, no. 1, pp. 94-101, Jan 1 2008.

[194] S. Jaeger, K. Palaniappan, C. S. Casas-Delucchi, and M. C. Cardoso, "Classification of Cell Cycle Phases in 3d Confocal Microscopy Using Pcna and Chromocenter Features," in *Proceedings of the Seventh Indian Conference on Computer Vision, Graphics and Image Processing*, 2010, pp. 412-418.

[195] I. Ersoy, F. Bunyak, V. Chagin, M. C. Cardoso, and K. Palaniappan, "Segmentation and Classification of Cell Cycle Phases in Fluorescence Imaging," in *International Conference on Medical Image Computing and Computer-Assisted Intervention*, 2009, pp. 617-624: Springer.

[196] D. Padfield, J. Rittscher, N. Thomas, and B. Roysam, "Spatio-Temporal Cell Cycle Phase Analysis Using Level Sets and Fast Marching Methods," (in English), *Medical Image Analysis,* vol. 13, no. 1, pp. 143-155, Feb 2009.

[197] T. H. Du, W. C. Puah, and M. Wasser, "Cell Cycle Phase Classification in 3d in Vivo Microscopy of Drosophila Embryogenesis," in *BMC Bioinformatics*, 2011, vol. 12, no. 13, pp. 1-9: Springer.

[198] I. Goodfellow, Y. Bengio, A. Courville, and Y. Bengio, *Deep Learning* (no. 2). MIT press Cambridge, 2016.

[199] M. Z. Alom *et al.*, "The History Began from Alexnet: A Comprehensive Survey on Deep Learning Approaches," *arXiv preprint arXiv:1803.01164,* 2018.

[200] Y. Nagao, M. Sakamoto, T. Chinen, Y. Okada, and D. Takao, "Robust Classification of Cell Cycle Phase and Biological Feature Extraction by Image-Based Deep Learning," *Molecular Biology of the Cell,* vol. 31, no. 13, pp. 1346-1354, Jun 15 2020.

[201] H. Narotamo, M. S. Fernandes, J. M. Sanches, and M. Silveira, "Interphase Cell Cycle Staging Using Deep Learning," in *2020 42nd Annual International Conference of the IEEE Engineering in Medicine & Biology Society (EMBC)*, 2020, pp. 1432-1435: IEEE.

[202] E. C. Jensen, "Use of Fluorescent Probes: Their Effect on Cell Biology and Limitations," (in English), *Anat Rec (Hoboken),* vol. 295, no. 12, pp. 2031-2036, Dec 2012.

[203] M. Tan and Q. Le, "Efficientnet: Rethinking Model Scaling for Convolutional Neural Networks," in *International Conference on Machine Learning*, 2019, pp. 6105-6114: PMLR.

[204] B. Baheti, S. Innani, S. Gajre, and S. Talbar, "Eff-Unet: A Novel Architecture for Semantic Segmentation in Unstructured Environment," in *Proceedings of the IEEE/CVF Conference on Computer Vision and Pattern Recognition Workshops*, 2020, pp. 358-359.

[205] P. Eulenberg *et al.*, "Reconstructing Cell Cycle and Disease Progression Using Deep Learning," (in English), *Nature Communications,* vol. 8, no. 1, p. 463, Sep 6 2017.

[206] T. Henser-Brownhill, R. J. Ju, N. K. Haass, S. J. Stehbens, C. Ballestrem, and T. F. Cootes, "Estimation of Cell Cycle States of Human Melanoma Cells with Quantitative Phase Imaging and Deep Learning," in *2020 IEEE 17th International Symposium on Biomedical Imaging (ISBI)*, 2020, pp. 1617-1621: IEEE.

[207] G. Pedrali-Noy, S. Spadari, A. Miller-Faures, A. O. Miller, J. Kruppa, and G. Koch, "Synchronization of Hela Cell Cultures by Inhibition of DNA Polymerase Alpha with Aphidicolin," *Nucleic Acids Research,* vol. 8, no. 2, pp. 377-387, Jan 25 1980.

[208] H. T. Ma and R. Y. Poon, "Synchronization of Hela Cells," in *Cell Cycle Synchronization*: Springer, 2011, pp. 151-161.

[209] H. Zhao, P. H. Brown, and P. Schuck, "On the Distribution of Protein Refractive Index Increments," *Biophysical Journal,* vol. 100, no. 9, pp. 2309-2317, May 4 2011.

[210] S. van der Walt *et al.*, "Scikit-Image: Image Processing in Python," *PeerJ,* vol. 2, p. e453, 2014.

[211] D. Lin, G. Chen, D. Cohen-Or, P.-A. Heng, and H. Huang, "Cascaded Feature Network for Semantic Segmentation of Rgb-D Images," in *Proceedings of the IEEE international conference on computer vision*, 2017, pp. 1311-1319.

[212] A. Chaurasia and E. Culurciello, "Linknet: Exploiting Encoder Representations for Efficient Semantic Segmentation," in *2017 IEEE Visual Communications and Image Processing (VCIP)*, 2017, pp. 1-4: IEEE.

[213] X. Li, H. Chen, H. Qi, Q. Dou, C. W. Fu, and P. A. Heng, "H-Denseunet: Hybrid Densely Connected Unet for Liver and Tumor Segmentation from Ct Volumes," *IEEE Transactions on Medical Imaging,* vol. 37, no. 12, pp. 2663-2674, Dec 2018.

[214] V. Badrinarayanan, A. Kendall, and R. Cipolla, "Segnet: A Deep Convolutional Encoder-Decoder Architecture for Image Segmentation," *IEEE Transactions on Pattern Analysis and Machine Intelligence,* vol. 39, no. 12, pp. 2481-2495, Dec 2017.

[215] F. Milletari, N. Navab, and S.-A. Ahmadi, "V-Net: Fully Convolutional Neural Networks for Volumetric Medical Image Segmentation," in *2016 fourth international conference on 3D vision (3DV)*, 2016, pp. 565-571: IEEE.

[216] T.-Y. Lin, P. Goyal, R. Girshick, K. He, and P. Dollár, "Focal Loss for Dense Object Detection," in *Proceedings of the IEEE international conference on computer vision*, 2017, pp. 2980-2988.

[217] C. H. Sudre, W. Li, T. Vercauteren, S. Ourselin, and M. J. Cardoso, "Generalised Dice Overlap as a Deep Learning Loss Function for Highly Unbalanced Segmentations," in *Deep Learning in Medical Image Analysis and Multimodal Learning for Clinical Decision Support*: Springer, 2017, pp. 240-248.

[218] X. Li, X. Sun, Y. Meng, J. Liang, F. Wu, and J. Li, "Dice Loss for Data-Imbalanced Nlp Tasks," *arXiv preprint arXiv:1911.02855,* 2019.

[219] P. Goyal *et al.*, "Accurate, Large Minibatch Sgd: Training Imagenet in 1 Hour," *arXiv preprint arXiv:1706.02677,* 2017.

[220] T. He, Z. Zhang, H. Zhang, Z. Zhang, J. Xie, and M. Li, "Bag of Tricks for Image Classification with Convolutional Neural Networks," in *Proceedings of the IEEE Conference on Computer Vision and Pattern Recognition*, 2019, pp. 558-567.

[221] I. Loshchilov and F. Hutter, "Sgdr: Stochastic Gradient Descent with Warm Restarts," *arXiv preprint arXiv:1608.03983,* 2016.

[222] R. K. Bista *et al.*, "Quantification of Nanoscale Nuclear Refractive Index Changes During the Cell Cycle," *Journal of Biomedical Optics,* vol. 16, no. 7, p. 070503, Jul 2011.

[223] Y. Rivenson, Y. Zhang, H. Gunaydin, D. Teng, and A. Ozcan, "Phase Recovery and Holographic Image Reconstruction Using Deep Learning in Neural Networks," (in English), *Light: Science & Applications,* vol. 7, no. 2, p. 17141, Feb 23 2018.

[224] Y. L. Luo, L. Z. Huang, Y. Rivenson, and A. Ozcan, "Single-Shot Autofocusing of Microscopy Images Using Deep Learning," (in English), *ACS Photonics,* vol. 8, no. 2, pp. 625-638, Feb 17 2021.

[225] S. He, K. T. Minn, L. Solnica-Krezel, M. A. Anastasio, and H. Li, "Deeply-Supervised Density Regression for Automatic Cell Counting in Microscopy Images," *Medical Image Analysis,* vol. 68, p. 101892, Feb 2021.

[226] K. Kawaguchi, L. P. Kaelbling, and Y. Bengio, "Generalization in Deep Learning," *arXiv preprint arXiv:1710.05468,* 2017.

[227] C. Zhang, S. Bengio, M. Hardt, B. Recht, and O. Vinyals, "Understanding Deep Learning Requires Rethinking Generalization," *arXiv preprint arXiv:1611.03530,* 2016.

[228] M. Roberts *et al.*, "Common Pitfalls and Recommendations for Using Machine Learning to Detect and Prognosticate for Covid-19 Using Chest Radiographs and Ct Scans," (in English), *Nature Machine Intelligence,* vol. 3, no. 3, pp. 199-217, Mar 2021.

[229] N. Sambasivan, S. Kapania, H. Highfill, D. Akrong, P. Paritosh, and L. M. Aroyo, ""Everyone Wants to Do the Model Work, Not the Data Work": Data Cascades in High-Stakes Ai," in *proceedings of the 2021 CHI Conference on Human Factors in Computing Systems*, 2021, pp. 1-15.